

# **Investigation of Thermoelectric Properties of Ruthantes Pyrochlore and A new Si-based High Entropy Pyrochlore**



**Project report submitted towards partial fulfillment of**

**M.S degree programme**

**by**

**Rupesh Kumar**

**20202015**

**Thesis Advisor: Dr. Surjeet Singh**

**Professor**

**Department of Physics**

**Indian Institute of Science Education and Research Pune**

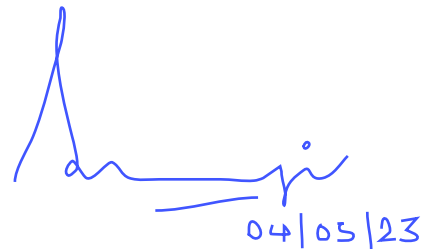


## *Certificate*

This is to certify that the thesis titled '**Investigation of Thermoelectric Properties of Ruthantes Pyrochlore and A new Si-based High Entropy Pyrochlore**' towards the partial fulfillment of the M.S. Degree programme at the Indian Institute of Science Education and Research (IISER), Pune represents the study/work carried out by Rupesh Kumar at IISER Pune under the supervision of Dr. Surjeet Singh, Professor, Department of Physics during the academic year 2022-2023.

*Rupesh Kumar*

**Signature of Student**



**Signature of Supervisor**

**Date:** 03/05/2023

**Place:** IISER Pune

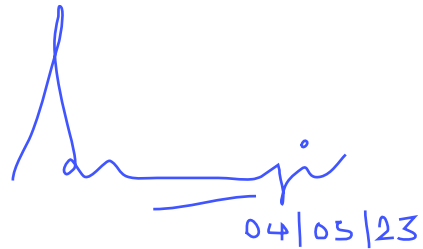


## **Declaration**

I hereby declare that the matter embodied in the report titled '**Investigation of Thermoelectric Properties of Ruthantes Pyrochlore and A new Si-based High Entropy Pyrochlore**' are results of the work carried out by me at the Department of Physics, IISER Pune, under the supervision of Dr. Surjeet Singh and the same has not been submitted elsewhere for any other degree.

*Rupesh Kumar*

**Signature of the Student**



04/05/23

**Signature of the Supervisor**

**Date:** 03/05/2023

**Place:** IISER Pune



*This thesis is dedicated to my parents.....*





## Acknowledgment

I am immensely grateful to express my sincere appreciation to my supervisor, Dr. Surjeet Singh, for his unwavering guidance, support, and invaluable insights throughout my project. His unwavering commitment and willingness to engage in open discussions and provide constructive feedback have been instrumental in shaping my research work. Under his tutelage, I have learned the art of thinking creatively, identifying research gaps, and asking challenging questions that have contributed significantly to my academic growth. I would also like to extend my heartfelt gratitude to Sagar for his invaluable contributions in teaching me solid-state synthesis, XRD, TGA-DSC, and operating an image furnace during my first year. I would also like to thank Dibyata, Navita, and Ankit for their consistent guidance, insightful discussions, and unwavering support during the course of my project. I am sincerely thankful to IISER Pune for providing such a nice infrastructure and atmosphere. I would like to thank Nilesh, Anil, Sudheer, Kartikeyan, and all other technical staff and housekeeping staff at IISER who helped me in my research. I would like to thank all administrative staff, especially Ranjan Kishor, Swapnil, Prabhakar, and Ashwini. A special thanks to Dean Academics Dr. Girish Ratnaprakhi for all kinds of administrative discussion and help. I am thankful to funding agencies IISER Pune and for economic support from IISER Pune and Infosys Pvt. Ltd. A special thanks to all my lab mates Dibyata, Navita, Nashra, Sagar, Ankit, Dinesh, Lalith, Pankaj, Arindam, Visakh, Vijayalaxmi and all. Dinesh, you are excellent, thanks for your expert suggestions while purchasing electronic gadgets. Also thanks to our past members Dr.Sourabh, Appu, and Siddhant. I would also like to thank Dr. Luminita mam. I learned a lot from all of you. I would like to thank all my colleagues, friends, and juniors at IISER Pune. I would like to thank Prabha, Circuit, Dewashish and Rohit, and all other friends outside Pune for their continuous suggestions, discussion, motivation, and fun. A special thanks to Prabha for her financial support throughout my career whenever I got stuck, especially at the time of admission at SXC Ranchi and IISER Pune. I learned a lot of things outside of physics, especially fitness (sorry for the same because I fail to maintain the same), and how to take care of someone else. Although my gratitude cannot be fully expressed in words, I am aware that this is only the beginning of our journey together, and we have a long road ahead of us. Sadanand whom I called circuit by love,

thanks man for standing with me always at the happy and worst time in my life, you are a person with zero attitudes, and infinite supportive nature always. I pray to God for your happy life ahead. We had many fights in the last 15 years but still, we are best friends, and nephews and know each other more than anyone else in this universe. Also, thank Mota for all your support in the last few years. I would also like to thank Sumit sir, Sanjay sir, Nusrat Ahmad mam, and Mitesh sir for their continuous guidance and motivation while preparing for IIT JAM. Lastly, I would like to thank my family for their endless love, support, and everything that they have invested in me for my career and for encouraging me every time to do anything in my life without any pressure in spite of their bad financial condition. Overall, I am incredibly grateful to everyone who has contributed to my academic and personal growth, and I hope to continue learning and growing under their guidance and support.



## Abstract

The pyrochlore system has a general formula of  $A_2B_2O_7$ , where A is typically a rare earth and B is a transition metal ion. It crystallizes in a face-centered cubic structure with space group Fd-3m. The structure consists of interpenetrating corner-shared tetrahedron networks made up of  $A^{3+}$  and  $B^{4+}$  ions. If either A or B happens to be magnetic, the system generally shows strong geometrical frustration. The Geometrical frustration arises when the magnetic interactions are incompatible with the lattice symmetry. For example, antiferromagnetically coupled spins on a triangular or tetrahedral motif.

Recently, the iridates family of pyrochlore has garnered a lot of attention due to its novel ground state, which can be adjusted through chemical doping at the A site. Other interesting features under discussion include the metal-to-insulator transition, magnetic transition at low temperatures, and anomalous lattice contraction. The competition between three energy scales, namely, spin-orbit interaction, onsite Coulomb repulsion, and crystal field splitting energy, plays a crucial role in determining the Weyl semimetallic ground state, making these systems both interesting and challenging to investigate.

This study aims to explore the Ruthenates series with  $Ru^{4+}$  at the B site. Ruthenate Pyrochlores with 4d transition metal ions on the B site are of huge interest because of their electronic properties, which can be tuned by altering the A site element. We synthesized four compounds of the  $(Eu_{1-x}Bi_x)_2Ru_2O_7$  series with 0%, 2%, 3.5%, and 100% Bi doping at the A site using conventional solid-state synthesis. After structural analysis, we conducted some thermoelectric measurements to evaluate their performance for a thermoelectric application, which are discussed in a separate chapter.

As the second part of my thesis, I worked on High entropy pyrochlores(HEP). In recent years, HEP has gained significant interest due to its ultra-low thermal conductivity, high stability at high temperatures, and high coefficient of thermal expansion. Therefore, it is considered a promising material for thermal barrier coatings (TBC), particularly in new high-temperature gas

turbine engines. The main objective in this part of the thesis is to synthesize some high entropy pyrochlores and prove the concept of entropy-stabilized phase using the thermal reversibility method. We attempted to synthesize  $A_2(\text{Ti}_{0.2}\text{Zr}_{0.2}\text{Hf}_{0.2}\text{Si}_{0.2}\text{Ce}_{0.2})_2\text{O}_7$ , where  $A = \text{Nd}, \text{Dy}$  and ;  $\text{Dy}_2(\text{Ti}_{0.2}\text{Zr}_{0.2}\text{Hf}_{0.2}\text{Si}_{0.2}\text{Sn}_{0.2})_2\text{O}_7$ , and  $\text{Dy}_2(\text{Ti}_{0.25}\text{Zr}_{0.25}\text{Hf}_{0.25}\text{Si}_{0.25})_2\text{O}_7$  using traditional solid-state synthesis. We carried out a detailed structural characterization of the synthesized sample and measure their thermal conductivity up to high temperatures (873K).

## List of Figures

**Fig 1.1:** showing a thermal conductivity comparison between different pyrochlore and high entropy pyrochlore.

**Fig 1.2:** The pyrochlore structure showing corner-shared tetrahedron of B site cations [13].

**Fig 1.3: (a)** Geometric frustration arising due to antiferromagnetic arrangement of spin on a triangular lattice, **(b)** a three-dimensional analogous of the triangular lattice.

**Fig 1.4:** Frustration in water ice and spin ice **(a)** In the case of water ice, the hydrogen ions tend to be positioned near one of their two neighboring oxygen ions, and each oxygen ion is typically surrounded by two hydrogen ions that are closer to it than to any adjacent oxygen ions **(b)** In spin ice, the orientation of the spins is either towards or away from the center of the tetrahedron. Each tetrahedron must have two spins pointing inwards and two spins pointing outwards, and this arrangement is strictly constrained [15].

**Fig 1.5:** Octahedral crystal field environment around the transition metal site (B- site).

**Fig 1.6:** Showing the crystal field orbital splitting of an octahedral structure.

**Fig 1.7:** Hubbard model for the half-filled case, where terms have their usual meaning.

**Fig1.8:** Showing terminological hierarchy often used for a material having compositional disorder on an ordered lattice[16].

**Fig 1.9:** Variation of calculated configurational entropy with a number of elements [16].

**Fig 2.1:** (a) Four mirror image furnaces at IISER Pune. (b) showing the close view of four mirrors and the rod of the sample which is hanging inside the quartz tube. (c) a photograph of the rod inside the furnace while sintering at high temperatures.

**Fig 2.2:** (a) X-ray diffraction instrument Bruker, D8 Advance diffractometer at IISER Pune, and a photograph of the setup showing the essential components of the diffractometer [18]. (b) Schematic representation of Bragg's law.

**Fig 2.3:** FESEM Ultra Zeiss plus facility at IISER Pune.

**Fig 2.4:** Showing the working of Scanning electron microscopy where the terms have their usual meaning [19].

**Fig 2.5:** Linseis LSR 3 setup [20].

**Fig 2.6:** Image showing the Seebeck coefficient measurement in a schematic diagram [20].

**Fig 2.7:** Image showing the resistivity measurement in a schematic diagram [20].

**Fig 2.8:** (a) The Laser flash analyzer 1000 by Linseis (b) showing the schematic design inside the LFA system [21].

**Fig 2.9:** showing the basic principle of thermal diffusivity measurement [21].

**Fig 3.1:** Showing powder XRD after each sintering.

**Fig 3.2:** (a) XRD after quenching from the image furnace. (b) XRD of the sample collected.

**Fig 3.3:** showing Elemental mapping.

**Fig 3.4:** Energy spectrum of all different elements.

**Fig 4.1:** (a) XRD graph after 12hr of sintering. (b) XRD graph after 44hr of sintering.

\

**Fig 4.2:** Rietveld refinement of the powder X-Ray diffraction pattern.

**Fig 4.3:** Morphology of the sample sintered for 12hr at different magnification scales.

**Fig 4.4:** Shows the elemental mapping of the sample after 12 hr sintering.

**Fig 4.5:** shows the morphology of the sample after sintering it for 44hr. The first five images show the morphology of the outer surface.

**Fig 4.6:** Elemental mapping of the sample.

**Fig 4.7:** Energy spectrum of a different element.

**Fig 4.8:** Shows the XRD graph of the annealed sample.

**Fig 4.9:** (a) Zoomed XRD peak before and after annealing. (b) Gaussian fitting of the peak corresponds to an annealed sample.

**Fig 4.10:** Thermal conductivity as measured from room temperature to 873K.

**Fig 5.1:** XRD graph of final compounds with different compositions.

**Fig 5.2:** (a) Variation of lattice parameter with Bi doping in %. (b) zoom view of (222) peak for all compounds.

**Fig 5.3:** (a) X=0, (b) X=0.02, (c) X=1, FESEM images. Grain size increases with Bi doping.



**Fig 5.4:** Corrected thermal conductivity variation with temperature with different X with 10% of the error bar.

**Fig 5.5:** Shows the variation of electrical conductivity for all samples.

**Fig 5.6:** Variation of thermopower S with temperature for different X.

**Fig 5.7:** Variation of zT with temperature for all compounds.

**Fig A.1:** Powder XRD after 16hr of sintering.

**Fig A.2:** (a) Morphology of the sample at different magnifications (b) Elemental mapping (c) EDX at a different area and atomic % of the various element over the same area shown in the table on the right.

**Fig A.3:** Powder XRD after 48hrs of sintering.

**Fig A.4:** (a) Morphology at different magnification scales (b) Elemental mapping.

**Fig A.5** Temperature-dependent on thermal conductivity.

## List of Table

**Table 2.1:** Table showing the precursors used with company name and their purity %.

**Table 3.1:** Showing elements with their respective atomic % present in the sample.

**Table 4.1:** Table showing all the goodness of fit parameters obtained using Rietveld refinement from the powder XRD.

**Table 4.2:** This table shows the atomic% of various elements at the point labeled spectrum 6 in the figure shown on the right.

**Table 4.3:** Table shows the atomic % of various elements in the area shown in Figure 4.6.

# Contents

**Declaration**

**Acknowledgments**

**Abstract**

**List of Figures**

**List of Tables**

<b>1 Introduction</b>	21
1.1 The Pyrochlore Structure	23
1.2 Geometrical Frustration in Pyrochlore	25
1.3 Spin Ice	26
1.4 Different kinds of competing interactions in pyrochlore systems	27
1.4.1 Crystal Field Effects	27
1.4.2 Spin-Orbit Coupling	29
1.4.3 Electron-Electron Correlation	29
1.5 The High Entropy Stabilised	31
1.5.1 Thermal Reversibility	33
1.5.2 Entropy Stabilised Pyrochlore	33
<b>2 Experimental Techniques</b>	35
2.1 Synthesis	35
2.1.1 Four Mirror Optical Float Zone Image Furnace	37
2.2 Structural and composition characterization	38
2.2.1 Powder X-Ray Diffraction	38
2.2.2 Scanning Electron Microscopy and Energy Dispersive Spectroscopy	40
2.3 The Physical Properties Measurement Systems	43

2.3.2 Linseis LSR 3	43
2.3.3 Laser Flash Analyzer	45
<b>3 Dy<sub>2</sub>M<sub>2</sub>O<sub>7</sub> (M = Ti<sub>0.2</sub> Zr<sub>0.2</sub> Hf<sub>0.2</sub> Sn<sub>0.2</sub> Si<sub>0.2</sub>)</b>	48
3.1 Synthesis Method	48
3.2 Structural characterization	48
3.2.1 Powder X-Ray Diffraction	48
3.2.2 SEM & EDX	50
3.3 Summary	52
<b>4 Dy<sub>2</sub>M<sub>2</sub>O<sub>7</sub> (M = Ti<sub>0.2</sub> Zr<sub>0.2</sub> Hf<sub>0.2</sub> Si<sub>0.2</sub> Ce<sub>0.2</sub>)</b>	53
5.1 Sample Synthesis	53
5.2 Sample Characterization	53
5.3 Thermal Reversibility and high entropy stabilized defect Fluorite	60
5.4 Thermal Conductivity Measurements	61
5.5 Summary	62
<b>5 Effect of Bi substitution on Eu<sub>2</sub>Ru<sub>2</sub>O<sub>7</sub></b>	63
5.1 Synthesis and structural characterization	63
5.1.1 Lattice parameter variation in (Eu <sub>1-x</sub> Bi <sub>x</sub> ) <sub>2</sub> Ru <sub>2</sub> O <sub>7</sub>	64
5.2 Thermoelectric Properties Measurement, Results, and Discussion	66
<b>6 Summary and Outlook</b>	71
<b>Appendix A Dy<sub>2</sub>M<sub>2</sub>O<sub>7</sub> (M = Ti<sub>0.25</sub> Zr<sub>0.25</sub> Hf<sub>0.25</sub> Si<sub>0.25</sub>)</b>	73
A.1 Synthesis and Characterization	73
A.2 Results and Summary	78
<b>Bibliography</b>	80

# Chapter 1

## Introduction

### Overview:

In condensed matter physics, transition metal oxides have continued to attract significant attention due to their unique structural, magnetic, and electronic properties. These oxides exist in a variety of structures. Here we focus on  $A_2B_2O_7$  (where A is generally a rare earth and B a transition metal ion) which is a family of oxides called the pyrochlores. The name pyrochlore is due to its similarity with the structure of the mineral  $\text{NaCaNb}_2\text{O}_6\text{F}$ , which is pyrochlore. The system has a cubic crystal structure with space group  $\text{Fd-}3\text{m}$  (227). Among other factors, the choice of combination of A and B site cations in the pyrochlore system is limited by the field of stability which is given by the ratio of their ionic radii i.e,  $R_A/R_B$ . For pyrochlore structure, their ratio varies from 1.46 to 1.78 wherein below 1.46 the structure is favored, as, defect fluorite for example, in  $\text{Dy}_2\text{Zr}_2\text{O}_7$  where the ratio of  $\text{Dy}^{3+}$  and  $\text{Zr}^{4+}$  ion is  $1.42\text{\AA}$ . On the other hand,  $\text{Dy}_2\text{Ti}_2\text{O}_7$  crystallizes in a pyrochlore structure with a  $\text{Dy}^{3+}$  and  $\text{Ti}^{4+}$  ratio of  $1.69\text{\AA}$ . Above  $R_A/R_B = 1.78$  the structure is no more cubic pyrochlore[1].

The magnetic properties of pyrochlore materials have also been the focus of intense research in recent years. The A-site cations in pyrochlore materials are typically magnetic rare earth ions, while the B-site cations are typically non-magnetic transition metals. This results in exotic magnetic ground states, ranging from spin ice state for example  $\text{Dy}_2\text{Ti}_2\text{O}_7$ ,  $\text{Ho}_2\text{Ti}_2\text{O}_7$  &  $\text{Nd}_2\text{Mo}_2\text{O}_7$ , where the magnetic moments form an arrangement analogous to the arrangement of  $\text{H}^+$  in common water ice to spin glass ground state in  $\text{Y}_2\text{Mo}_2\text{O}_7$ , and a possible spin liquid ground state of  $\text{Tb}_2\text{Ti}_2\text{O}_7$ [1,2]. The study of the magnetic properties of pyrochlore materials has led to the discovery of new phenomena such as magnetic monopoles, which are topologically stable excitations that behave like particles with a magnetic charge.

The electronic properties of pyrochlore materials have also been studied extensively. The rare earth ions in pyrochlore materials have partially filled with 4f electrons, which leads to a variety of interesting phenomena such as Kondo physics and heavy fermion behavior. The study of the electronic properties of pyrochlore materials has led to the discovery of new materials with

interesting electronic properties such as the topological insulator  $\text{Bi}_2\text{Te}_2\text{O}_7$ , weyl- semimetal  $(\text{Eu}_{1-x}\text{Bi}_x)_2\text{Ir}_2\text{O}_7$ , [3], etc.

In the first part of my thesis, I will present some work on ruthenate pyrochlores which is a subfamily of the (+3, +4) class of pyrochlore. This class of material is interesting to explore the thermal properties because the  $\text{A}_2\text{Ru}_2\text{O}_7$  ( $\text{A}=\text{Ln}, \text{Y}, \text{Bi}$ ) [4] compounds show the metal-insulator transition upon bigger cationic doping at the A site. The electrical conductivity is governed by the Ru-O-Ru bond framework through Ru-4d & O-2p states, which can be controlled by the degree of overlap between the states followed by controlling the size of rare earth cations. With increasing the A site cationic radii the Ru-O-Ru bond angle increases which leads to flattening the bond, increasing the orbital overlap, increasing the bandwidth, and decreasing the electrical resistivity.

In this thesis, we present the study of  $(\text{Eu}_{1-x}\text{Bi}_x)_2\text{Ru}_2\text{O}_7$ . We chose this material due to our belief that the insulating nature of  $\text{Eu}_2\text{Ru}_2\text{O}_7$  would result in a high Seebeck coefficient, while proximity to a metal-insulator transition (MIT) through Bi doping at a site would lead to sufficiently low electrical resistivity, thus resulting in good thermoelectric performance. We have conducted measurements of the thermoelectric properties and compared them with those of other reported oxides which are further discussed in Chapter 5.

Pyrochlore compounds have also been studied for various applications such as catalysis, fuel cell electrodes, and nuclear waste storage. The interest in pyrochlore materials as nuclear waste arises from their high chemical stability, which prevents the leaching of radioactive isotopes. The materials also have a high radiation tolerance, allowing them to maintain their structural integrity even in the presence of high radiation levels [6,7,8]. The pyrochlore system currently lacks empirical rules for entropic stabilization, which is a new area of research [9,10]. At high temperatures, the pyrochlores with  $R_A/R_B$  ratio very close to 1.46 tend to show pyrochlore to Fluorite transition, and it is crucial to examine trends with temperature.

The second part of this thesis involves synthesis, characterization, and thermal conductivity measurement of entropy-stabilized pyrochlore  $\text{Dy}_2(\text{Ti}_{0.2}\text{Zr}_{0.2}\text{Hf}_{0.2}\text{Ce}_{0.2}\text{Si}_{0.2})_2\text{O}_7$  and  $\text{Dy}_2(\text{Ti}_{0.25}\text{Zr}_{0.25}\text{Hf}_{0.25}\text{Si}_{0.25})_2\text{O}_7$ .

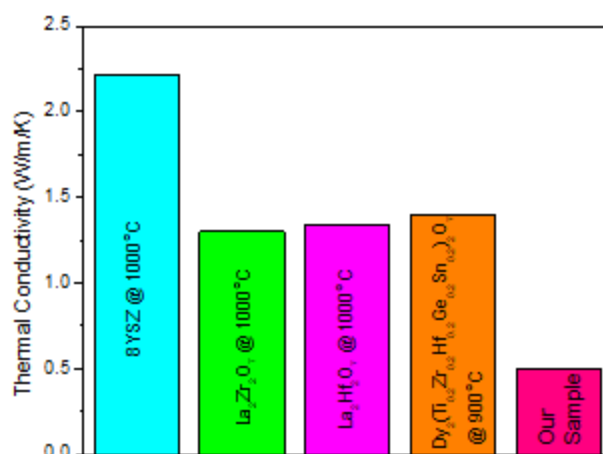


**Fig 1.1:** showing a thermal conductivity comparison between different pyrochlore and high entropy pyrochlore[8,12,27]

In the case of  $\text{Dy}_2(\text{Ti}_{0.2}\text{Zr}_{0.2}\text{Hf}_{0.2}\text{Ge}_{0.2}\text{Sn}_{0.2})_2\text{O}_7$ , the expected paramagnetic ground state was observed at low temperatures due to the high magnetic moment of Dy (around  $10 \mu_B$ )[12]. Since  $\text{Dy}_2\text{Ti}_2\text{O}_7$  has a spin ice ground state at low temperatures it will be interesting to investigate the ground state of high entropy pyrochlore based on Dy. The disorder of the B site through the incorporation of five different elements with varying ionic sizes and masses should have implications for the spin in the ground state. The highly disordered B-site should also influence the lattice thermal conductivity. The pyrochlore compound to start exhibit a low-lattice thermal conductivity. The disorder at the B-site is expected to lower it further, close to the amorphous limit. Consequently, it will be intriguing to investigate the low-temperature ground state of this compound.

## 1.1 The Pyrochlore Structure

The general formula of pyrochlore oxides can be written as  $\text{A}_2\text{B}_2\text{O}_6\text{O}'$ , where A and B are rare earth and transition metal cations respectively. Pyrochlore structure can be visualized in many ways for example fluorite structure, defect pyrochlore structure, two interpenetrating networks of  $\text{B}_2\text{O}_6$  and  $\text{A}_2\text{O}'$ , etc. Pyrochlore stabilized in space group Fd-3m with space group number 227

while defect pyrochlore in Fm-3m. The figure below shows a pyrochlore structure seen as corner-sharing tetrahedra of B site ions.

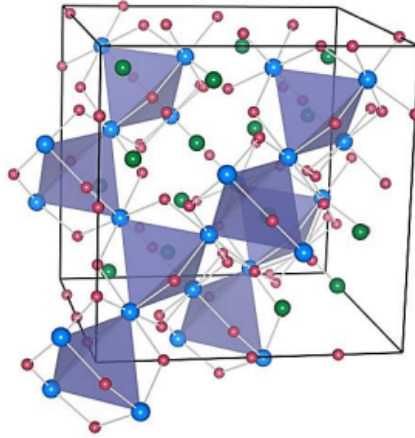


**Fig 1.2:** The pyrochlore structure showing corner-shared tetrahedron of B site cations [13].

It can also be visualized as a combination of two polyhedra, namely an 8-fold coordinated cube ( A site ) and a 6-fold coordinated octahedron ( B site ). The shape of these polyhedra is tuned by  $x$ , the position parameter of the oxygen location 48f site[1].

Theoretically,  $x$  varies from 0.3125 to 0.375, and for  $x = 0.3125$ , [1] the B site is surrounded by a perfect octahedron while the A site is surrounded by a distorted polyhedron. On the other hand, as the  $x$  parameter comes closer to 0.375, the B-site octahedron becomes distorted and the A-site polyhedra starts becoming more cubic.

The pyrochlore structure contains spins on the corners of the tetrahedra, which can result in geometrical frustration. This means that it is impossible to minimize the interaction energy for all lattice sites simultaneously, resulting in a degenerate manifold of ground states rather than a single stable ground state configuration. This can lead to magnetic phenomena such as spin ice and spin liquid. However, even small perturbations can cause instabilities in these systems.

The effect of geometric frustration on the ground states of strongly correlated pyrochlore systems is an area of active research, as it can lead to novel electronic properties. In particular, 4d and 5d



transition metal pyrochlore oxides exhibit interesting transport properties such as the anomalous Hall effect in  $\text{Nd}_2\text{Mo}_2\text{O}_7$  and  $\text{Pr}_2\text{Ir}_2\text{O}_7$ , superconductivity in  $\text{Cd}_2\text{Re}_2\text{O}_7$ , metal-insulator transition (MIT) in  $\text{Cd}_2\text{Os}_2\text{O}_7$ ,  $\text{Eu}_2\text{Ir}_2\text{O}_7$ ,  $\text{Sm}_2\text{Ir}_2\text{O}_7$ . These phenomena provide insight into the interplay between geometric frustration and electronic properties, which is an important topic in condensed matter physics.

Although the choice of A and B site cations in pyrochlore varies from (+2, +5) to (+3, +4), and a mixture of both. In our case, we will only deal with (+3, +4) types of pyrochlore.

## 1.2 Geometrical Frustration in Pyrochlore

Geometrical frustration is a phenomenon that occurs when a crystal lattice arrangement creates competing or contradictory constraints that cannot all be satisfied simultaneously to find a unique lowest energy state. This frustration arises due to the geometry of the lattice, and for a spin-lattice system, it is called magnetic geometrical frustration. The main source of such competition and frustration in the system is different energy exchange parameters[14].

A very general example of a frustrated lattice is a two-dimensional triangular lattice. In the case of an antiferromagnetic arrangement, a third spin is always in a dilemma to satisfy the antiferromagnetic ordering with both of the other two spins simultaneously. This results in frustration in the system, as the third spin cannot find a stable configuration that satisfies all constraints. The picture below illustrates this scenario.

The concept of geometrical frustration is not limited to the two-dimensional triangular lattice, but it also occurs in other crystal structures. One example is the pyrochlore structure, where the arrangement of metal cations in the lattice leads to more complex geometrical frustration, which results in interesting physical properties such as spin ice  $\text{Dy}_2\text{Ti}_2\text{O}_7$ [11] and spin glasses, etc. High entropy pyrochlore is a more complex version of the pyrochlore structure, where 4, 5, or even more cations are substituted simultaneously at the A or B site. This leads to a more intricate geometrical spin frustration[11]. At low temperatures, it becomes interesting to observe how the overall ground state evolves in response to the increased complexity.

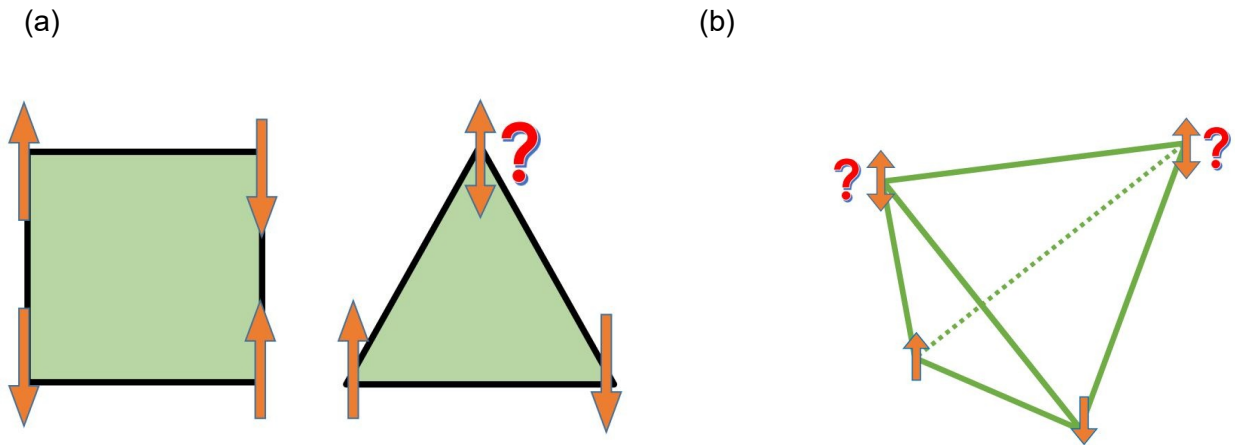


**Fig 1.3:** (a) Geometric frustration arising due to antiferromagnetic arrangement of spin on a triangular lattice,(b) a three-dimensional analogous of the triangular lattice.

Also, the addition of multiple cations at the A or B site results in more disorder and frustration in the system, leading to a more complicated energy landscape. This can lead to the emergence of new phenomena such as spin-glass behavior, magnetic relaxation, etc. The presence of multiple cations in the lattice also increases the degree of configurational entropy, which can enhance the stability of the high entropy pyrochlore structure.

### 1.3 Spin Ice

The concept of frustrated systems originated from the study of water ice, where bond disorder leads to residual entropy at extremely low temperatures. Linus Pauling identified the macroscopically degenerate ground state of spin ice in which the bonding arrangement could be achieved in six alternate ways. This theoretical model was experimentally established in 1997 by Harris and coworkers in the pyrochlore oxide  $\text{Ho}_2\text{Ti}_2\text{O}_7$ , where the term spin ice was coined. This compound and its counterpart  $\text{Dy}_2\text{Ti}_2\text{O}_7$  represent the classical spin-ice system in which the magnetism arises from the A-site ion, while  $\text{Ti}^{4+}$  is non-magnetic. Due to the large moment of the rare-earth ions, the applied fields of several Teslas are too weak to turn the A-site ions away from their local quantization axes. As a result, strong quantum effects are absent in these compounds.

However, other rare-earth pyrochlores like  $\text{Yb}_2\text{Ti}_2\text{O}_7$  and  $\text{Er}_2\text{Ti}_2\text{O}_7$ , where the effective spin at the A site is  $1/2$  and  $3/2$ , respectively, are highly frustrated and prone to quantum effects. The spins in these compounds are controlled by exchange coupling rather than long-range dipolar interactions. Recent studies suggest that  $\text{Yb}_2\text{Ti}_2\text{O}_7$  may host an unusual quantum critical point at larger magnetic fields and support a quantum spin liquid ground state in a moderate magnetic field. Thus, pyrochlores represent an intriguing class of materials with complex magnetic behavior arising from the interplay of lattice geometry and exchange interactions.

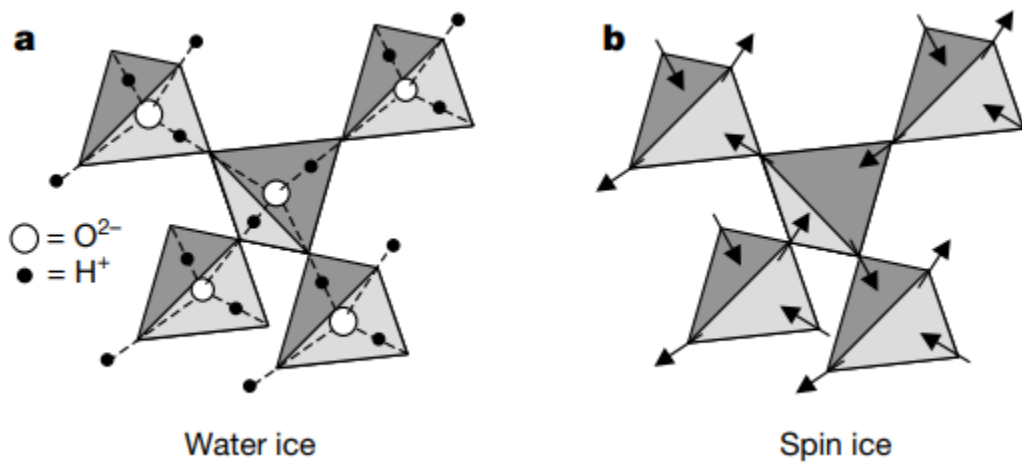


**Fig 1.4:** Frustration in water ice and spin ice **(a)** In the case of water ice, the hydrogen ions tend to be positioned near one of their two neighboring oxygen ions, and each oxygen ion is typically surrounded by two hydrogen ions that are closer to it than to any adjacent oxygen ions **(b)** In spin ice, the orientation of the spins is either towards or away from the center of the tetrahedron. Each tetrahedron must have two spins pointing inwards and two spins pointing outwards, and this arrangement is strictly constrained [15].

## 1.4 Different kinds of competing interactions in pyrochlore system

### 1.4.1 Crystal Field Effects

Crystal field theory explains the impact of neighboring ligand atoms on the electronic structure of a central ion in a crystal. The theory models neighboring orbitals as negative point charges,

while ligand field theory expands on this by focusing on the d orbitals on the central ion and their overlap with surrounding ions. The size and nature of crystal field effects depend on the symmetry of the local environment. Octahedral environments are commonly studied, as transition metal ions in many compounds sit at the center of an octahedron with ions such as oxygen on each corner. Crystal field effects in this scenario are mainly due to electrostatic repulsion from negatively charged electrons in the oxygen orbitals.

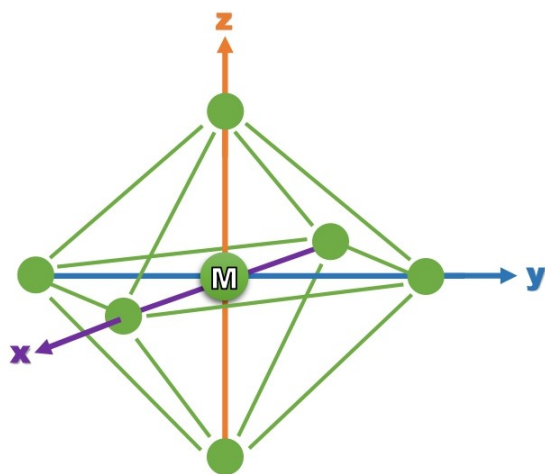


**Fig 1.5:** Octahedral crystal field environment around the transition metal site (B- site).

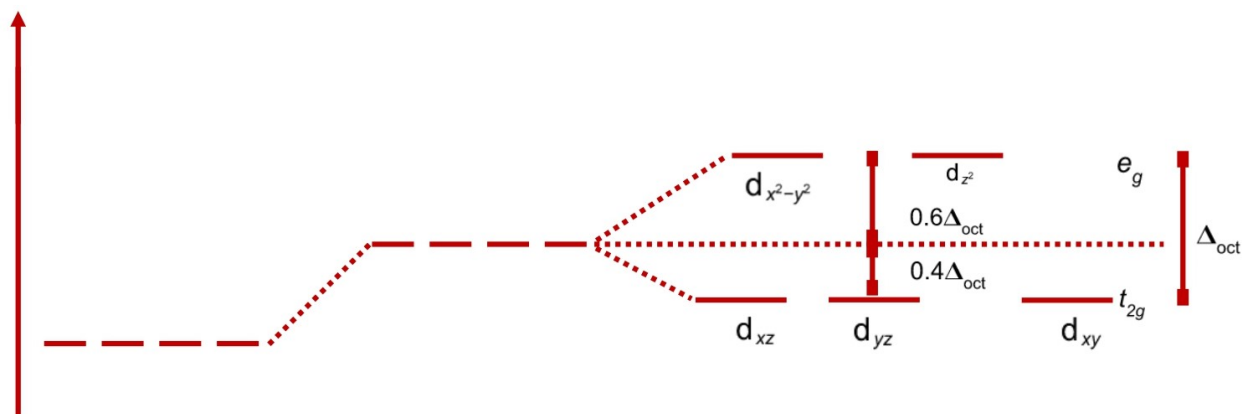


**Fig 1.6:** Showing the crystal field orbital splitting of an octahedral structure.

In the case of a regular octahedron, the orbitals  $d_{x^2-y^2}$  and  $d_{z^2}$  (as shown above in Figure 1.7) point toward the oxygen ions, which raises their electrostatic potential energy compared to  $d_{xy}$ ,  $d_{yz}$ , and  $d_{zx}$  orbitals. Therefore, in an octahedral crystal field, the d-orbitals are split into a group of doublet ( $e_g$ ) and a triplet ( $t_{2g}$ ).

The size of the splitting,  $\Delta_{\text{oct}}$  compared to the energy required to pair electrons in the same orbital, determines whether a system will assume a high or low spin state, with high spin states corresponding to higher magnetic moments[14]. Rare earth ions are also surrounded by oxygen ions, but the 4f orbitals, which are partially filled, are more protected from the repulsive effects of the crystal field by the  $5s^2$  and  $5p^6$  electrons. The impact of the crystal field increases as we move from 3d to 5d transition metal ions, as the orbitals become more exposed to the crystal field due to their increased spread.

### 1.4.2 Spin-Orbit Coupling

Spin-orbit coupling is the interaction between the spin and orbital angular momentum of an electron revolving around a nucleus. As the electron moves around the nucleus, it creates a magnetic field, which affects the spin. The effect of spin-orbit coupling is more pronounced in heavier elements, as it is directly proportional to the atomic number  $Z^4$ . In lighter atoms, L-S coupling is treated as a small perturbation that has no such splitting effect on the energy level corresponding to different J values. However, in heavier elements, L-S coupling plays a significant role and causes further splitting of each J value, giving rise to the hyperfine structure [14].

### 1.4.3 Electron-Electron Correlation

Electronic correlation is a fundamental concept in condensed matter physics that explains how electrons in a solid can behave differently from an ideal, non-interacting gas-like system. This is due to the repulsion between electrons, resulting from their charge and spin.

In non-interacting systems, electrons move independently and occupy available energy states according to the Pauli exclusion principle. However, in interacting systems, electrons can affect

one another's motion and distribution due to mutual repulsion, resulting in electronic correlation. This effect is particularly important in materials with strongly interacting electrons, such as transition metal oxides.

The simplest example of electronic correlation is the Coulomb repulsion between two electrons occupying the same energy level, known as the on-site Coulomb repulsion ( $U$ ) or Hubbard repulsion. Electronic correlation modifies the electronic band structure, resulting in occupied states with higher energies and unoccupied states with lower energies. This can cause the system to become insulating, even if it is expected to be metallic according to the band theory of solids. Such insulators are called Mott insulators, and they tend to order antiferromagnetically to lower the kinetic energy of the system. A metal-insulator transition (MIT) occurs when the on-site Coulomb repulsion ( $U$ ) becomes comparable to the bandwidth ( $W$ ).

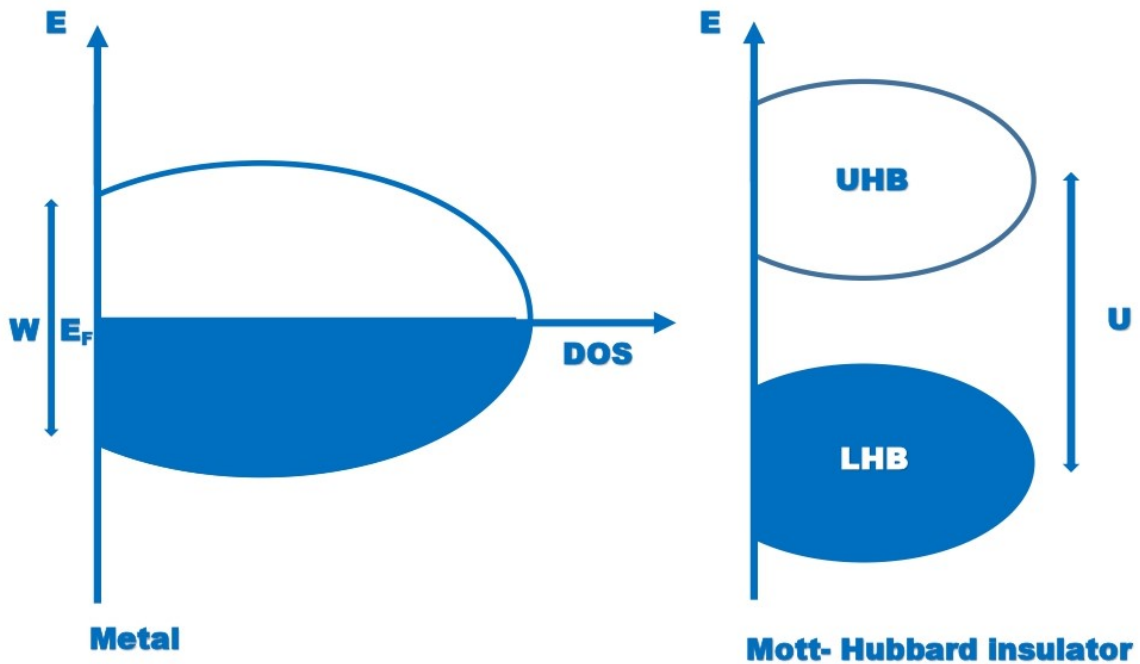


**Fig 1.7:** Hubbard model for the half-filled case, where terms have their usual meaning.

The single-particle (Hartree-Fock approximation) model describes the behavior of each electron in a system using a single-particle wave function. This model works well for systems

with weak electron-electron interactions, such as noble gases. However, it breaks down for systems with stronger interactions, such as transition metals. The energy calculated using the Hartree-Fock approximation for a Mott insulator differs from the actual energy of the electron. This difference is known as correlation energy, which is a measure of the on-site Coulomb repulsion ( $U$ ). i.e higher the  $U$ , the higher will be the correlation energy. Such systems with High Correlation energy are called strong electron systems[14].

## 1.5 The High Entropy Stabilised System

In the realm of materials science, there are three distinct types of materials systems that have emerged in recent years: compositionally complex, high entropy, and stabilized entropy. A compositionally complex system is characterized as one containing multiple elements in roughly equal proportions at the same site, which can lead to high configurational entropy. This entropy can contribute to achieving a minimum Gibbs free energy, particularly at high temperatures, and maybe the driving force behind the formation of a single-phase compound in entropy-stabilized oxides. One example of a compositionally complex system is high entropy alloys (HEAs), which are alloys that contain five or more principal elements in roughly equal proportions at the same site.

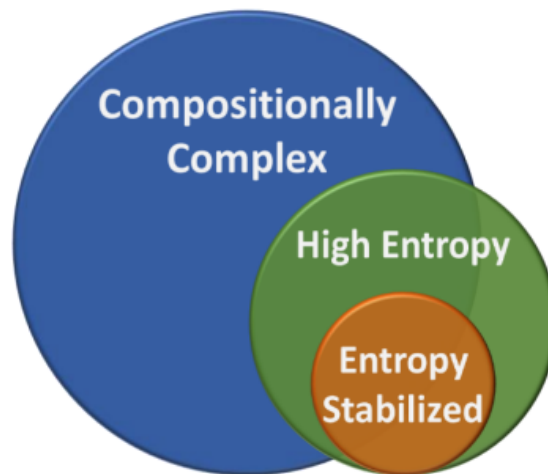


**Fig 1.8:** Showing terminological hierarchy often used for a material having compositional disorder on an ordered lattice[16].

The equation for the total configurational entropy for statistically ideal mixing in a crystal in a crystal is given by equation (i), where R represents the gas constant,  $m_j$  denotes the atoms per formula unit on the  $j$ th crystallographic site,  $x_{ij}$  is the mol fraction of species  $i$  on the  $j$ th crystallographic site. On the other hand, in high-symmetry metallic systems, such as fcc, bcc, or hcp metals, this equation simplifies to the single-lattice model given by equation (ii) below[16].

$$S_{\text{Configurational}} = - R \sum_{ij} m_j x_{ij} \ln x_{ij} \quad - (i)$$

$$S_{\text{Configurational}} = - R \sum_i x_i \ln x_i \quad - (ii)$$

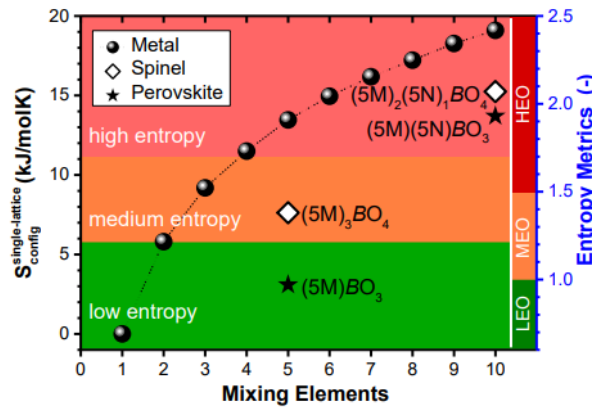


**Fig 1.9:** Variation of calculated configurational entropy with a number of elements [16].

In general, a system is considered entropy stabilized when its enthalpy of formation ( $\Delta H_f$ ) is positive, and its entropy of formation ( $\Delta S_f$ ) is positive and sufficiently large to result in a negative Gibbs free energy of formation (refer to equation (iii) ) at a certain temperature (T) or above it.

$$G = H - T S \quad - (iii)$$

The entropy of formation is typically  $\frac{ds}{dn_i} = R \ln X_i$  composed of two contributions,  $\Delta S_f = \Delta S_{\text{Thermal}} + \Delta S_{\text{config}}$ . If a compound's components are ordered (i.e.,  $S_{\text{config}} = 0$ ), and if the crystalline compound is perfectly disordered, then  $\Delta S_{\text{config}}$  can be  $\mu_i = \frac{dG}{dn_i}$  calculated



using equation (i). In phase equilibria, partial molar entropy  $\frac{ds}{dn_i} = R \ln X_i$  is a more crucial factor in determining phase stability than  $\Delta S_{\text{config}}$ , this is because the partial molar entropy, which is  $\mu_i = \frac{dG}{dn_i}$  determined under the ideal mixing assumption, has a direct relationship with the chemical potential and the chemical potential of the components present in a solution regulates the solubility limits and phase stability, making partial molar entropy a key factor in phase equilibrium[16].

These materials are often designed with specific properties in mind, such as high strength, improved corrosion resistance, or enhanced thermoelectric properties.

### 1.5.1 Thermal Reversibility

An entropy-stabilized system can exhibit thermal reversibility, where after annealing below its formation temperature for a long period, a secondary phase may emerge as seen by XRD peaks and SEM morphology. However, sintering the sample at high temperatures can lead to the system being stabilized again in a single phase. This phenomenon provides evidence for the stability of the entropy-stabilized system. The duration of annealing varies depending on the system, as the segregation dynamics can be low[17,12].

### 1.5.2 Entropy Stabilised Pyrochlore

High Entropy Stabilized Pyrochlore (HESP) is a type of crystal lattice stabilized by the high degree of configurational entropy generated by the random distribution of multiple cations at a particular site. Recently, Pascanut-Decorse et al. reported the first entropy-stabilized pyrochlore  $\text{Dy}_2(\text{Ti}_{0.2}\text{Zr}_{0.2}\text{Hf}_{0.2}\text{Ge}_{0.2}\text{Sn}_{0.2})_2\text{O}_7$  [12]. It is worth noting that  $\text{Dy}_2\text{Ge}_2\text{O}_7$  (stabilizes in tetragonal structure, although it stabilizes in pyrochlore only using high pressure and temperature) does not stabilize in the pyrochlore structure at ambient temperature and pressure, while  $\text{Dy}_2\text{Zr}_2\text{O}_7$  and  $\text{Dy}_2\text{Hf}_2\text{O}_7$  form the defect fluorite phase individually. By introducing an enthalpy penalty at the B site, entropic stabilization can be induced, leading to the system being stabilized in a high-symmetry state.

In our study, we have replaced 20% of the B site with Si, Ti, Zr, Hf, and Ce. Here,  $\text{Dy}_2\text{Si}_2\text{O}_7$  can not be stabilized in the pyrochlore structure. Furthermore, it will be interesting to see the ground state system at low temperatures and investigate the thermal properties at high temperatures for potential applications such as TBC, irradiation resistance, and more[12].

Further details regarding our work will be discussed in the subsequent chapters.

## Chapter 2

### Experimental Techniques

#### 2.1 Synthesis

Solid-state synthesis is a widely employed synthesis technique worldwide. Transition metal oxides, in particular, have a high melting point and require heating at elevated temperatures for extended periods, which may last several weeks. During sintering, precursor materials diffuse and undergo chemical reactions, resulting in the formation of the desired product. The process of diffusion also results in the reduction of voids between particles, leading to densification. Increasing the sintering temperature can accelerate the reaction rate, leading to the formation of the desired product in a shorter time.

The details of precursors used are given below-

Dy <sub>2</sub> O <sub>3</sub>	Alfa aesar 99.9%	TiO <sub>2</sub>	Sigma Aldrich 99.9%
Ho <sub>2</sub> O <sub>3</sub>	Sigma Aldrich 99.9%	SnO <sub>2</sub>	Sigma Aldrich 99.9%
Eu <sub>2</sub> O <sub>3</sub>		RuO <sub>2</sub>	
Y <sub>2</sub> O <sub>3</sub>	Alfa aesar 99.99%	GeO <sub>2</sub>	Alfa aesar 99.98%
Bi <sub>2</sub> O <sub>3</sub>			
ZrO <sub>2</sub>	Sigma Aldrich 99%	HfO <sub>2</sub>	Alfa aesar 99.9%
CeO <sub>2</sub>		SiO <sub>2</sub>	
MgO	Sigma Aldrich(99.99%)	CuO (Tenorite)	Alfa Aesar (99.995%)

(Rocksalt )			
ZnO (Wurtzite)	Sigma Aldrich (99.99%)	CoO (Rocksalt)	Alfa Aesar (99.998%)
NiO (Rocksalt)	Sigma Aldrich (99.99%)		

**Table 2.1:** Table showing the precursors used with company name and their purity %.

To obtain the desired product, stoichiometric amounts of precursor materials were thoroughly mixed, and rare-earth oxides were dried overnight to remove any trace of moisture. The resulting mixture was ground for 1-2 hours to obtain a homogeneous mixture. To enhance diffusion and maximize contact between powder grains, the powder mixture was pressed at nearly 9 tons in a hydraulic KBr press, resulting in a dense pellet. For high entropy pyrochlore, a hydraulic press was used to make rods a few centimeters in length with a pressure of around 70-75 MPa. The pellets and rods were then placed in an alumina crucible and fired in a high-temperature furnace, with the temperature varying depending on the sample. For example, the high entropy sample was fired at up to 1500°C, while Ruthenates pyrochlore was limited to 1050°C due to the volatile nature of RuO<sub>2</sub>. After each sintering cycle, the samples were reground and examined for their phase purity using x-ray diffraction. If unreacted precursors were detected, the sintering cycle was repeated until a single phase was obtained with intermediate grinding and pelletizing.

To minimize the loss of precursors, it is advisable to commence sintering at a lower temperature when dealing with volatile precursors. For instance, in the case of Bi-doped pyrochlore, we initiate sintering at 850°C.

On the other hand, the synthesis protocol for high entropy alloys differs somewhat from that of Ruthenates pyrochlore. Rather than slow cooling during sintering, air quenching is required to freeze the dynamics and obtain a single phase. However, air quenching at high temperatures above 1000°C poses a significant risk of damage.

To mitigate this risk, we have devised a novel approach to effectively quench the sample from such high temperatures. Specifically, we conducted the sintering of high entropy pyrochlore in a four-mirror optical float zone image furnace. We will elaborate on this under a separate subheading.

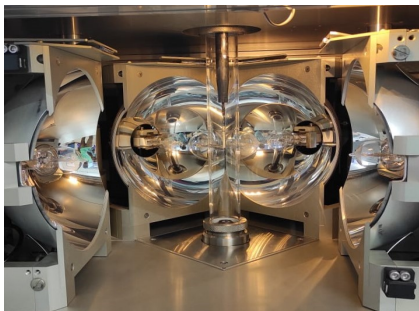
### 2.1.1 Four-Mirror Image Furnace

The four-mirror image furnace is primarily used for growing high-purity single crystals using a seed and feed made up of a polycrystalline sample of interest. However, in this thesis, we have employed the furnace solely for sintering our sample at high temperatures with air quenching at the end.

(a)



(b)



(c)

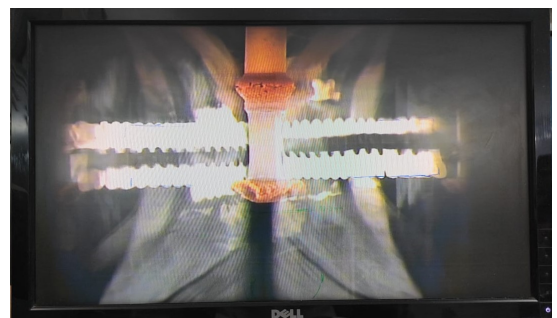


**Fig 2.1:** (a) Four mirror image furnaces at IISER Pune. (b) showing the close view of four mirrors and the rod of the sample which is hanging inside the quartz tube. (c) a photograph of the rod inside the furnace while sintering at high temperatures.

The furnace comprises four semi-ellipsoidal mirrors with halogen lamps located at their foci. The second focus of all the mirrors coincides with the vertical axis at the center of the furnace, where the light flux converges after reflecting off the mirrors. The large vertical temperature gradient along the axis facilitates high-temperature sintering from a polycrystalline cylindrical rod.

We utilized the FZ-T-10000-H-HR-I-VPM-PC model of the four-mirror optical image furnace, manufactured by Crystal System Corporation in Japan. It has a maximum operating temperature of approximately 2200°C, achievable by four 1000-watt halogen lamps. In our case, we used four 1000-watt lamps and operated at 65% of the power, equivalent to around 1600°C-1700°C

## **2.2 Structural and composition characterization**

### **2.2.1 Powder X-Ray Diffraction**

Powder X-ray diffraction is a powerful technique used to determine the crystal structure of a crystalline material. It involves exposing a powdered sample to X-rays and measuring the pattern of diffracted X-rays produced by the sample. The pattern of diffracted X-rays contains information about the atomic arrangement within the crystal structure of the sample in a specific atomic plane.

The principle involved in powder X-ray diffraction lies in Bragg's law, which states that the diffraction of X-rays by a crystal lattice occurs when the X-rays interact with the planes of atoms in the lattice in a way that their path difference equals an integer multiple of the wavelength of the X-Ray used, which can be written as-

$$2d\sin\theta = n\lambda$$

Where  $d$  is the interplanar spacing,  $\theta$  is the angle of incident x-rays with the plane of the sample,  $n$  is the order of diffraction and  $\lambda$  is the wavelength of the x-ray used.

In general, X-rays are generated from a target (say Cu in our case with wavelength  $1.5405 \text{ \AA}$ ) through a process known as an X-ray tube or X-ray generator. Electrons are accelerated towards the target by a high voltage, and when they collide with the target atoms in the anode, X-rays are emitted. The energy of the X-rays produced is determined by the difference in energy levels between the electronic shells involved in the transition, and the X-ray spectrum has characteristic peaks corresponding to the different transitions in the target atoms. For example,  $K\alpha$  and  $K\beta$  are the most intense peak in the characteristics spectrum corresponding to L and M shells to the innermost shell K respectively.

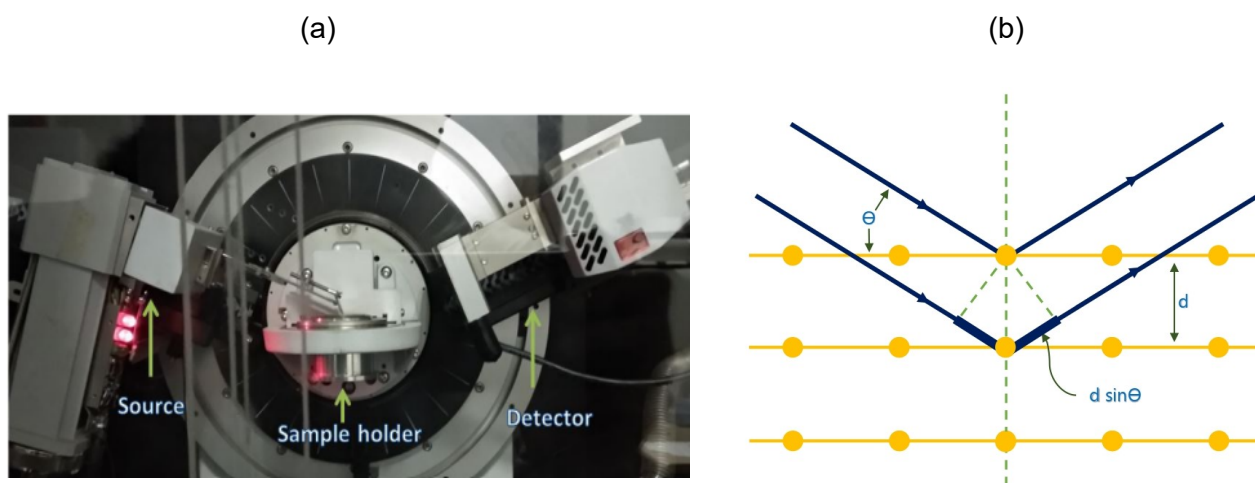


**Fig 2.2:** (a) X-ray diffraction instrument Bruker, D8 Advance diffractometer at IISER Pune, and a photograph of the setup showing the essential components of the diffractometer[18]. (b) Schematic representation of Bragg's law.

In a typical powder XRD experiment, a powdered sample is placed on a sample holder and then exposed to a beam of X-rays. The X-rays interact with the atoms in the crystal lattice and produce a pattern of diffracted X-rays that are collected by a detector. The pattern of diffracted X-rays is then analyzed using software programs to determine the crystal structure of the sample. One of the key advantages of PXRD is that it is a non-destructive technique, meaning that the sample is not destroyed during the analysis. This makes it an ideal technique for studying

materials that are rare or difficult to synthesize. Additionally, because PXRD is a bulk technique, it can be used to analyze a large number of samples quickly and efficiently.

For this study, room temperature Powder X-ray Diffraction was conducted using a Bruker D8 Advance Powder X-Ray Diffractometer. To begin, the prepared samples were ground into a fine powder and then mounted onto a glass slide. This prepared sample was then placed into the diffractometer. It is worth noting that the glass slide is amorphous and does not contribute to the XRD spectrum. The resulting diffraction patterns were then compared to the standard patterns recorded in a database provided by the International Centre for Diffraction Data (ICDD).

### **2.2.2 Scanning Electron Microscopy and Energy Dispersive Spectroscopy**

Scanning Electron Microscopy (SEM) is a widely used technique to see the morphology of a crystalline sample. It uses a focused beam of electrons to scan the surface of a sample and create an image with high resolution and magnification. In scanning electron microscopy, a sample is placed in a vacuum chamber and the electron beam is generated from an electron source, typically a tungsten filament, and accelerated by an electric field toward the sample. When the electrons hit the surface of the sample, they interact with the atoms and molecules of the material, producing various signals that can be detected and used to form an image.

The most commonly used signal in SEM imaging is secondary electrons, which are produced by the interaction of the incident electrons with the surface of the sample. These secondary electrons carry information about the morphology and topography of the sample surface and are collected from the detector to form an image of the sample

Energy Dispersive X-ray Spectroscopy (EDS) is a technique that is used with SEM to obtain information about the elemental composition of a sample. When secondary electrons are emitted from the surface of a sample, other electrons may transition to fill the vacancy, resulting in the production of X-rays. These X-rays have energy corresponding to the difference in energy levels between the electrons involved in the transition. Since the energy levels in atoms are unique, these X-rays are known as characteristic X-rays, and their wavelength is referred to as the



characteristic wavelength. EDS works by detecting these characteristic X-rays emitted by the sample, providing information about the elemental composition of the material.



**Fig 2.3:** FESEM Ultra Zeiss plus facility at IISER Pune.

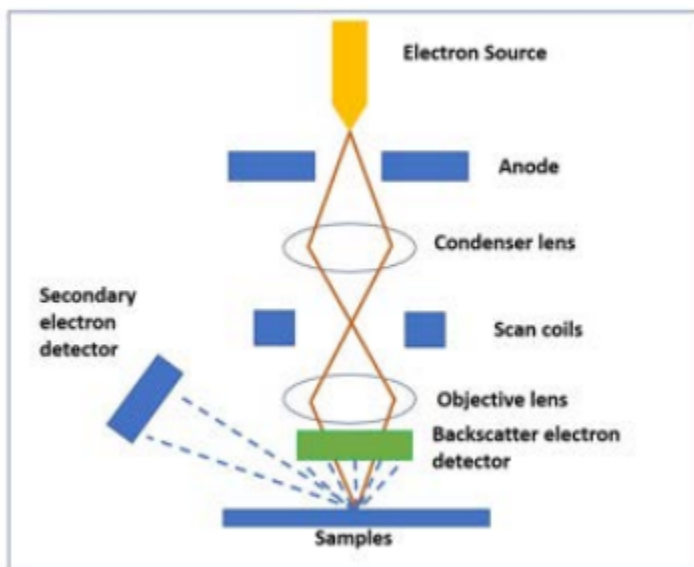


**Fig 2.4:** Showing the working of Scanning electron microscopy where the terms have their usual meaning [19].

Also since X-rays have high energy so one can penetrate the sample up to a good depth. In EDS, the X-rays are detected by a semiconductor detector, typically made of silicon or germanium, which converts the X-rays into electrical signals that can be analyzed by a computer. The resulting spectrum provides information about the elements present in the sample and their relative ratio.

While imaging the morphology of a sample, we typically use a low voltage, such as 3-5KeV. However, to obtain EDS spectra, a higher voltage is needed, usually around 15-20 KeV. In our case, EDS spectra were taken at 20KeV. However, we encountered an issue with the EDS detector detecting lighter elements. Therefore, when performing EDS, we refrain from including oxygen as it may affect the overall relative presence of other heavier elements in the sample.

The surface morphology and elemental composition of the synthesized samples were examined using a Zeiss Ultra Plus Scanning Electron Microscope. To prepare the samples, a section of each synthesized sample was wet-cut in Isopropyl Alcohol (IPA), polished using a Silica Carbide polishing paper of 1000 grid, sonicated for 30 minutes, and dried in an oven. The polished samples were then placed on double-sided carbon tape and mounted onto SEM stubs. Multiple points and areas on the surface were randomly chosen to record the surface morphology and elemental composition.

## 2.3 The Physical Properties Measurement Systems

The transport properties of the prepared samples were studied. For most of these measurements, we used LFA and LSR systems which are in our lab.

### 2.3.1 Linseis LSR 3

LSR is a powerful tool to measure the Seebeck coefficient and electrical resistivity of materials at high temperatures. The system works on the principle of the Seebeck effect, which is the phenomenon where a temperature difference across a material creates a voltage difference.



**Fig 2.5:** Linseis LSR 3 setup [20].

In our case, we have used the Linseis LSR 3 system consisting of a measurement probe that is placed in contact with the material being tested. The probe contains a heating element and a thermocouple, which are used to create a temperature gradient across the material. Here the heating is carried by halogen lamps. In order to measure the Seebeck coefficient, the Linseis LSR 3 system first heats the material to a predetermined temperature. Once the material has reached the desired temperature, the system measures the voltage generated by the Seebeck effect and calculates the Seebeck coefficient of the material. A basic phenomenon is also shown in the diagram below.

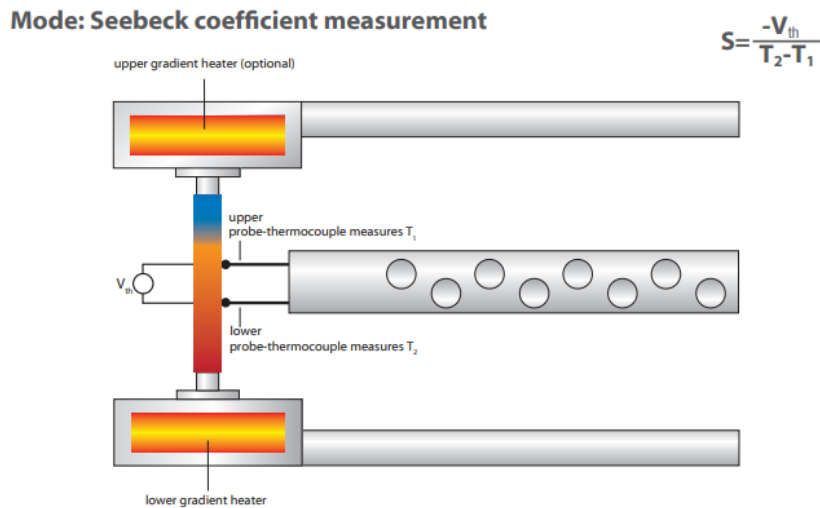


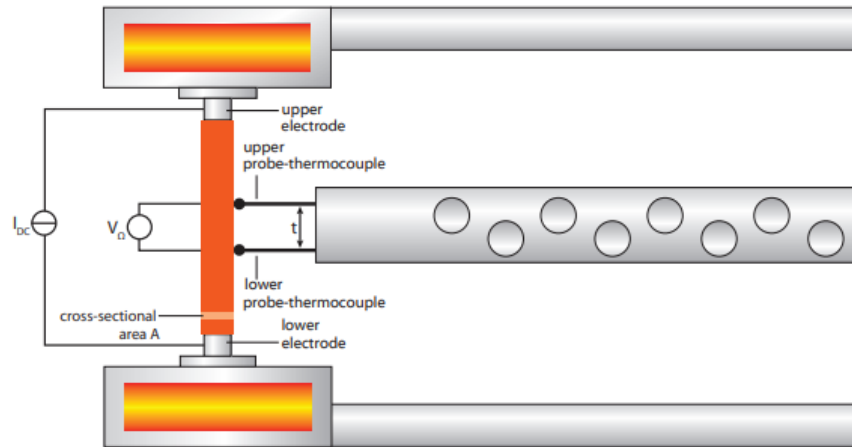
**Fig 2.6:** Image showing the Seebeck coefficient measurement in a schematic diagram [20].

While on the other hand in order to perform an electrical resistivity measurement, the Linseis LSR 3 system applies a known current to the material and measures the voltage drop across the material. Then by using the value of the sample area of the cross-section and its distance from the central probe system calculate the electrical resistivity of the material given by us.

The Linseis LSR 3 system is capable of measuring Seebeck coefficients and electrical resistivity over a wide temperature range, from room temperature up to 1000°C. This makes it useful for studying materials that are used in high-temperature applications, such as thermoelectric materials or materials used in power generation systems.

Mode: resistivity measurement

$$\rho = \frac{V_{\Omega}}{I_{DC}} \cdot \frac{A}{t}$$



Schematic of the LINSEIS Standard LSR measurement system

Fig 2.7: Image showing the resistivity measurement in a schematic diagram [20].

Well-polished and rectangular bar shape (of a few mm in length and thickness) samples were used to measure the above quantity and also all samples were measured in an inert atmosphere (Helium).

### 2.3.2 Laser Flash Analyzer

The LFA-1000 Linseis is a measurement system that utilizes the Laser Flash method to measure the thermal conductivity of materials at high temperatures. The measurement process involves recording the temperature rise as a function of time, which can be used to calculate the thermal diffusivity of the material. The thermal conductivity is then calculated by multiplying the thermal diffusivity with the material's specific heat capacity and density governed by the relation-

$$\kappa = D \cdot C_p \cdot \rho.$$

Laser flash is directed towards the bottom surface of the sample which raises the temperature of the top surface. Then the temperature of the top surface is detected by an IR

detector which is then used to calculate the thermal diffusivity of the system. The IR detector needs to cool using Liq N<sub>2</sub>, which was filled in the Dewar placed at the top of the device. It depends upon the thickness and half of the time ( $t_{1/2}$ ) to rise to obtain the maximum temperature on the top surface of the sample given by the formula  $D = 0.13879(L^2 / t_{1/2})$ . Although it works in ideal condition.

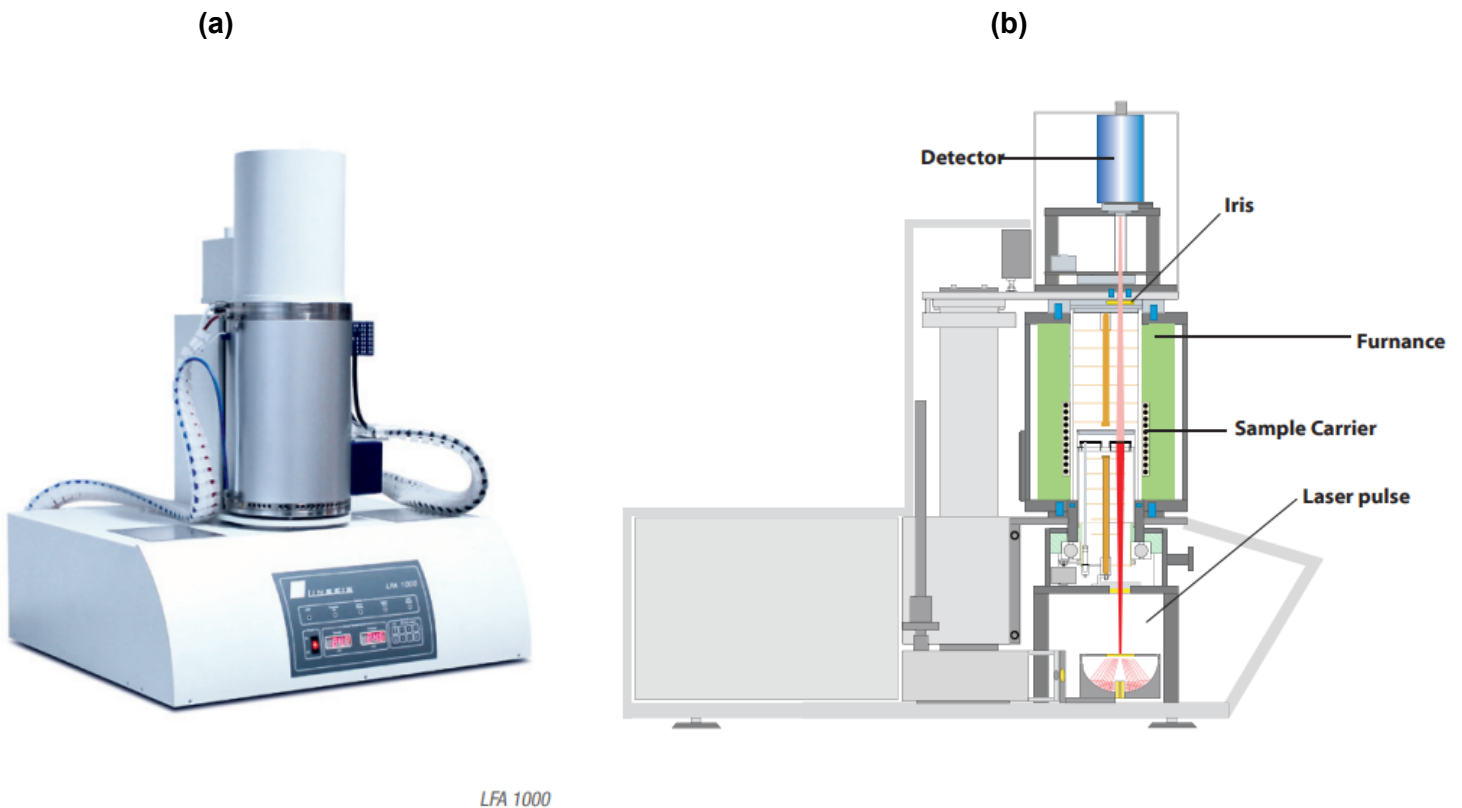


**Fig 2.8:** (a) The Laser flash analyzer 1000 by Linseis (b) showing the schematic design inside the LFA system [21].

To ensure accurate measurements, three readings are taken at each temperature, and data is only accepted if it has a good fitting greater than or equal to 96%. The sample chamber is evacuated and purged with helium gas before measurement to avoid oxidation, and the sample is coated with a graphite layer to homogenize heat diffusion and increase absorption efficiency. The sample chamber and Laser unit are cooled using continuous water flow using a chiller.

Various sources of errors can affect the accuracy of measurements, including errors in density estimation, specific heat obtained using the Dulong-Petit law, diffusivity measurements, and factors related to sample thickness, surface, heat loss, and data fitting. In the high entropy pyrochlore sample, the relative density was between 60-75% due to the highly porous sample. We have corrected our thermal conductivity using a formula to exclude the effect of the porosity factor discussed later in the chapter.

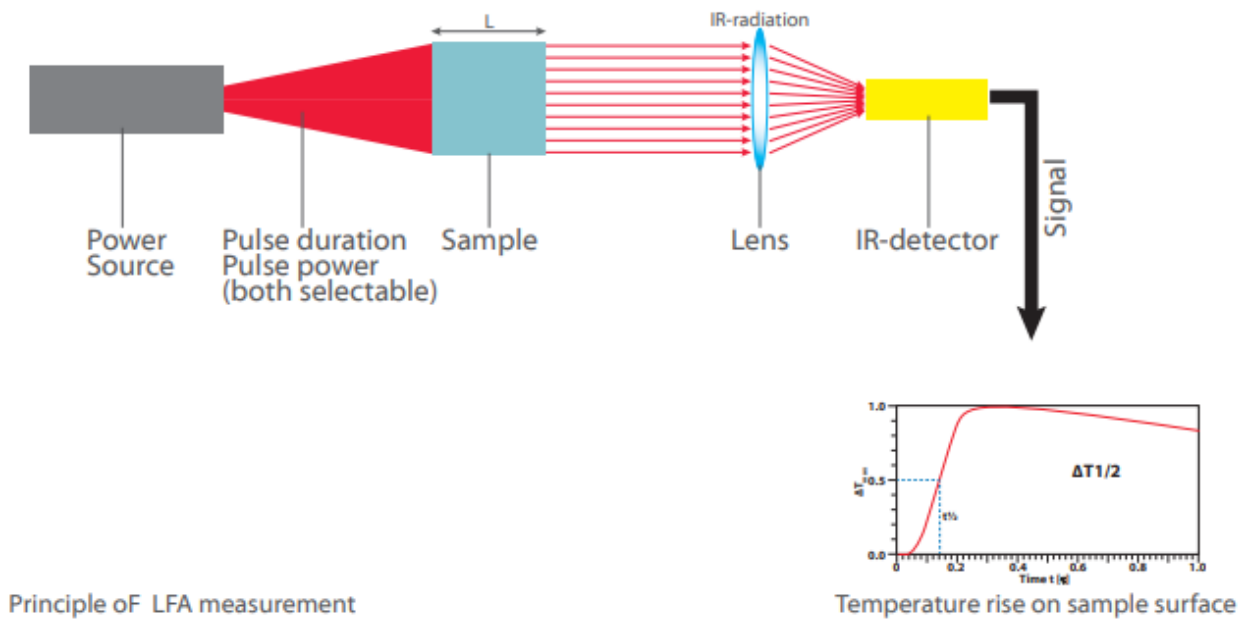
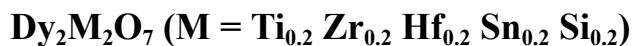


**Fig 2.9:** showing the basic principle of thermal diffusivity measurement [21].

## Chapter 3



### 3.1 Synthesis Method

The solid-state synthesis method was employed in this study, utilizing precursors including Dy<sub>2</sub>O<sub>3</sub> (Alfa Aesar at 99.9% purity), ZrO<sub>2</sub> (Sigma Aldrich at 99% purity), HfO<sub>2</sub> (Alfa Aesar at 99.9% purity), TiO<sub>2</sub> (Sigma Aldrich at 99.9% purity), SnO<sub>2</sub> (Sigma Aldrich at 99.9% purity), and SiO<sub>2</sub> (Alfa Aesar at 99.999% purity).

Stoichiometric amounts of these precursors were manually ground for one hour using a mortar and pestle. The resulting mixture was pelletized using a KBr press (13mm, 9 tons) and subjected to six consecutive sintering processes.

The sintering processes were conducted at different temperatures, starting with 1200°C, followed by 1400°C, 1500°C, and 1570°C, with intermediate grinding. Two additional sintering processes were carried out at 1350°C and 1500°C for 18 hours each because after 1570°C we thought these impurities may be of unreacted Dy<sub>2</sub>O<sub>3</sub> so we mixed 10g extra Dy<sub>2</sub>O<sub>3</sub> and sintered it again.

During the sintering processes, the sample underwent weight loss of 1.84%, 0.65%, 0.47%, 1.18%, and 0.84% at 1200°C, 1400°C, 1500°C, 1570°C, and 1350°C/1500°C, respectively. The color of the sample changed from white to yellow after 1500°C, and it became dense.

In a subsequent step, the same sample was sintered using an image furnace to obtain a single phase. To achieve this, air quenching was performed at 65% power of the lamps to arrest the dynamics and capture the single phase after 1hr of sintering time.

For this purpose, polycrystalline rods of the sample, consisting of Dy<sub>2</sub>(Ti<sub>0.2</sub>Zr<sub>0.2</sub>Hf<sub>0.2</sub>Sn<sub>0.2</sub>Si<sub>0.2</sub>)<sub>2</sub>O<sub>7</sub> with pyrochlore phase as well as impurity phase, were prepared. These rods were a few centimeters in length and 3.5g in weight.

### 3.2 Structural Characterization

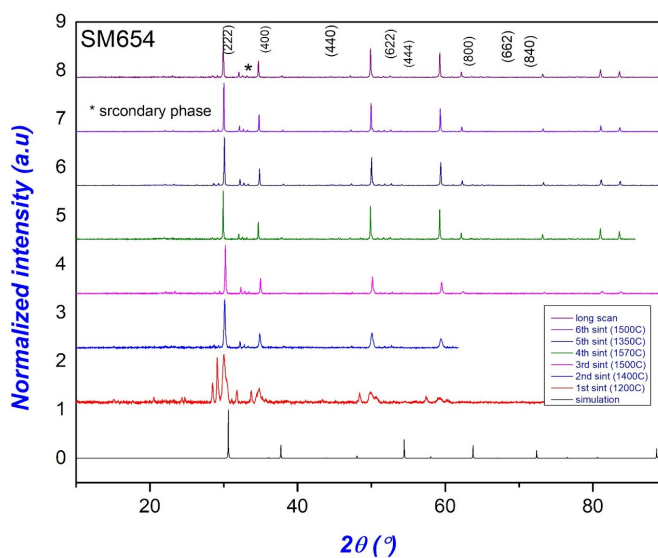
#### 3.2.1 Powder X-Ray Diffraction



To characterize the prepared samples, powder X-ray diffraction (XRD) was performed. The XRD plot presented below shows the results obtained for the  $\text{Dy}_2(\text{Ti}_{0.2}\text{Zr}_{0.2}\text{Hf}_{0.2}\text{Sn}_{0.2}\text{Si}_{0.2})_2\text{O}_7$  sample after various sintering processes.

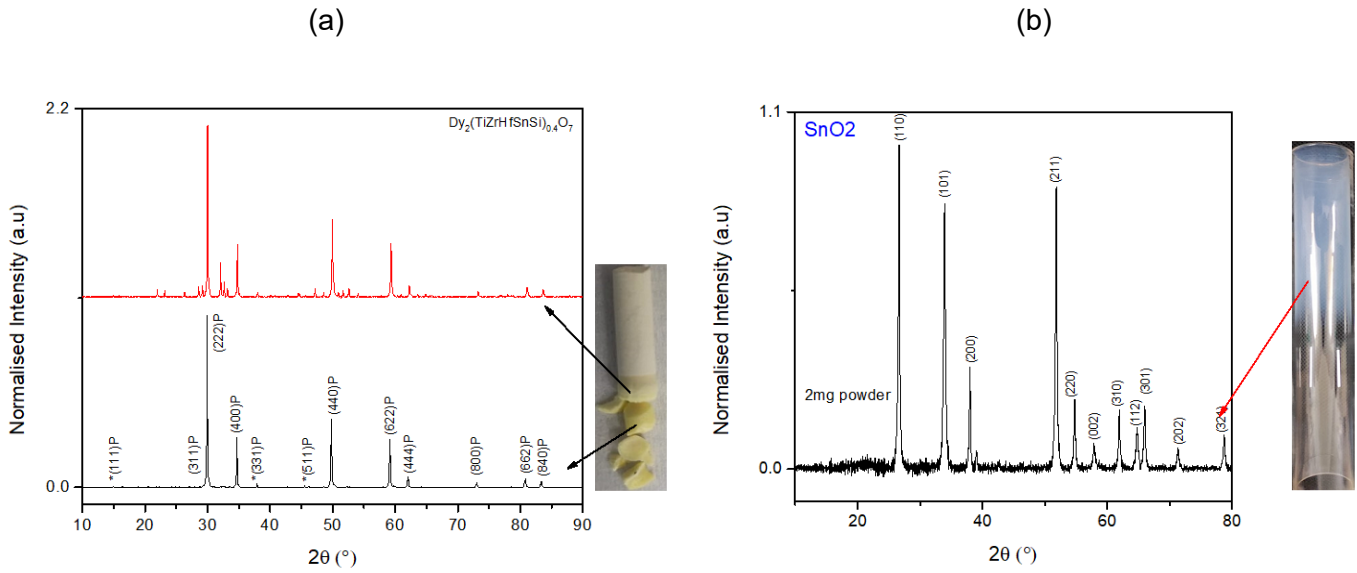
Upon sintering at  $1570^\circ\text{C}$  with slow cooling ( $250^\circ\text{C}$  per hour), a pyrochlore phase was obtained. However, the XRD plot showed the presence of some additional peaks of impurity, which are marked with an asterisk (\*) in the graph.

The X-ray diffraction (XRD) plot below illustrates the results obtained after air quenching the sample at 65% power for 0.5 hours. This XRD confirms the formation of a pyrochlore phase, with the impurity phase being almost completely suppressed. While on the other hand, the upper part of the sample shown by the arrow in Fig. 3.2 (a) confirms the pyrochlore phase has some impurities. It was expected because the upper part was at a lower temperature than the main zone part, which was not sufficient to form a single phase. We did the air quenching by just moving the upper shaft up within seconds by hand, meaning taking the sample (rod) out of the main heating point. Then upon cooling the furnace we move the upper shaft down back to collect the sample.



**Fig 3.1:** Showing powder XRD after each sintering.

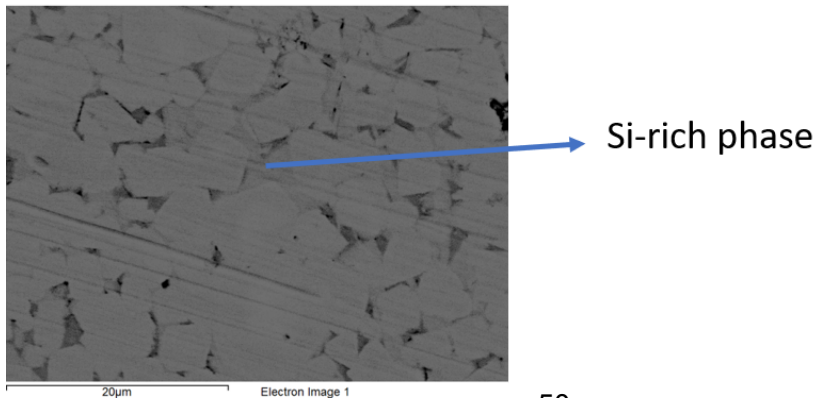
During the sintering process, some powder was collected, which was found to be SnO<sub>2</sub> upon analysis using XRD.



**Fig 3.2:** (a) XRD after quenching from the image furnace. (b) XRD of the sample collected.

### 3.2.2 SEM & EDX

The elemental mapping analysis of the single-phase part of the sample has verified the homogeneous distribution of the Dy element in the A site. However, a non-uniform distribution was observed for the B site. Additionally, the presence of an extra Si-rich phase was detected, which is consistent with the small secondary peaks observed in the X-ray diffraction pattern.



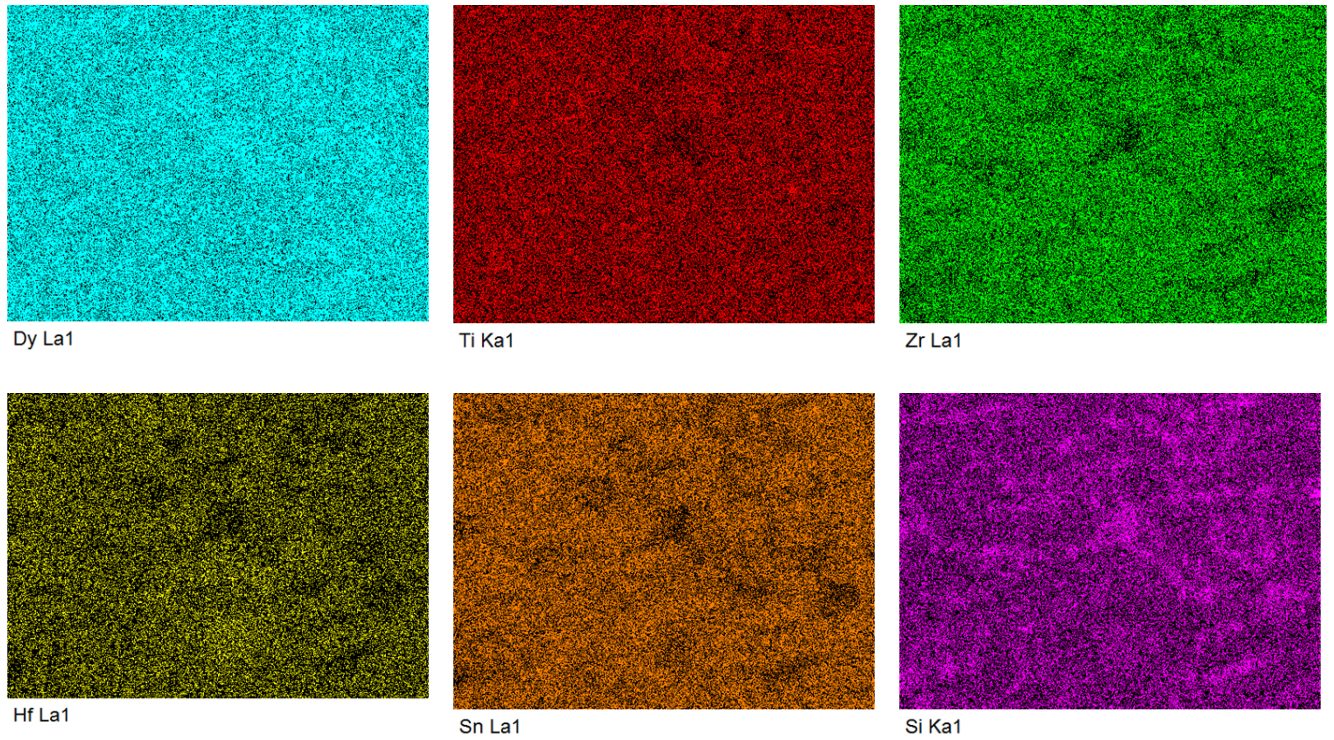


**Fig 3.3:** showing Elemental mapping.

The slight deviation in the elemental composition of a certain element can be attributed to the overlapping of energy spectra from different elements.

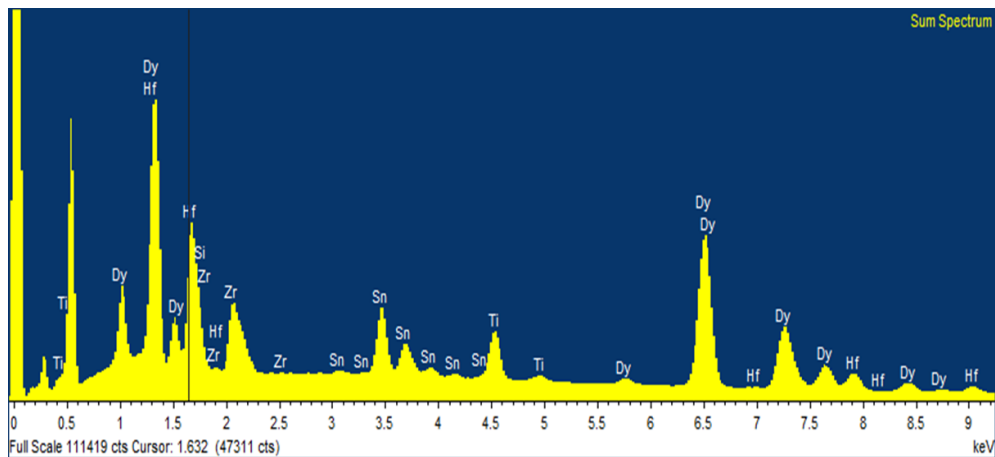


**Fig 3.4:** Energy spectrum of all different elements.

Element	Dy	Ti	Zr	Hf	Sn	Si
Atomic %	43.84	10.32	13.76	8.11	12.21	11.36

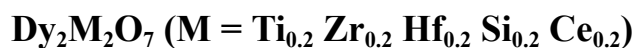
**Table 3.1:** Showing elements with their respective atomic % present in the sample.

### 3.3 Summary

Sintering in a muffle or box furnace followed by slow cooling always resulted in the formation of secondary phases that could easily be detected using powder XRD. However, when sintered in the image furnace at higher temperatures and upon subsequent quenching, a nearly single-phase sample could be obtained. However, the processing in the image furnace resulted in some loss of volatile SnO<sub>2</sub>

To further address the volatility issue of SnO<sub>2</sub>, we have explored the possibility of replacing it with CeO<sub>2</sub>. We hope that this substitution will allow us to increase the sintering time, thereby providing a longer duration for phase formation. We will discuss this strategy further in the upcoming chapter.

## Chapter 4



### 4.1 Sample Synthesis

All necessary precursors were thoroughly mixed and hand-ground for one and a half hours. The resulting mixture underwent the first sintering process at 1200°C, followed by two more sintering processes at 1400°C and 1500°C respectively. Between these sintering steps, the mixture was pelletized and hand-ground. After the third sintering process, we prepared rods of diameter 6mm and length few centimeters. To ensure the rods were dense enough, we sintered them at 1500°C for approximately 24 hours before transferring them to the image furnace.

The image furnace provides the unique capability of quenching the rods from very high temperatures, which is not possible using a regular furnace. We suspended the rod from the upper shaft of the furnace such that the lower end of the rod reached the convergence point of the light rays from the lamp. A rotation rate of 4-6 rpm was used to ensure temperature homogeneity conducted at 65% power for approximately 12 hours, followed by air-quenching. We did the air quenching by just moving the upper shaft up within seconds by hand, meaning taking the sample (rod) out of the main heating point. Then upon cooling the furnace we move the upper shaft down back to collect the sample same as discussed in Chapter 3 also.

Upon examination with SEM, we observed secondary phases of Si in the sample. To address this, we increased the sintering time to 44 hours, which resulted in a pure phase whose characterization details are given in the next section.

### 4.2 Sample Characterization

To verify that the sample consisted of a pure phase, we conducted powder X-ray diffraction (XRD) and scanning electron microscope-energy dispersive X-ray spectroscopy (SEM-EDX) analyses.

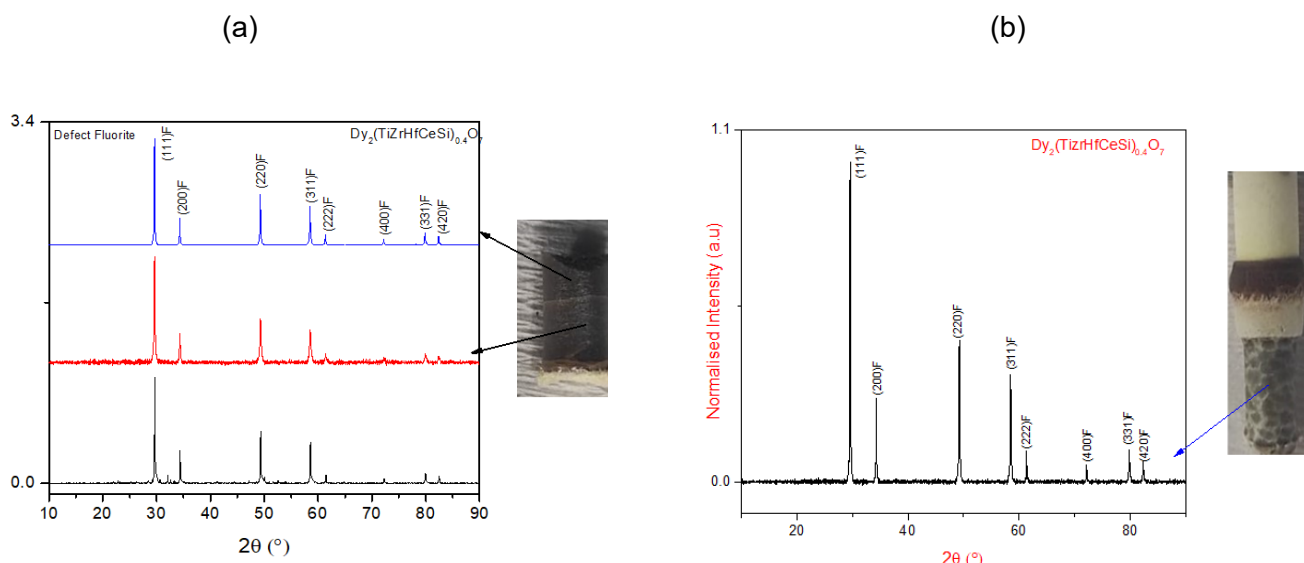


**Fig 4..1:** (a) XRD graph after 12hr of sintering. (b) XRD graph after 44hr of sintering.

The x-ray diffraction (XRD) analyses confirmed the presence of a pure defect fluorite phase, which was crystallized in the Fm-3m space group. Unlike the first experiment, the sintered rod in this experiment also showed a slight color variation, which we attributed to a slight loss of CeO<sub>2</sub> during the longer sintering period. However, a change in oxygen stoichiometry due to high-temperature sintering may also be the reason for the change of contrast.

Fig.4.2 below shows the Rietveld refinement of the X-Ray diffraction pattern of the synthesized Dy<sub>2</sub>(Ti<sub>0.2</sub>Zr<sub>0.2</sub>Hf<sub>0.2</sub>Ce<sub>0.2</sub>Si<sub>0.2</sub>)<sub>2</sub>O<sub>7</sub> compound with reliability factors as shown in the table, confirming that a single-phase cubic defect fluorite (space group Fd-3m) with a = 5.23 Å is obtained by quenching from high temperatures (T>1500°C). The exact temperature corresponding to the 65% lamp power used in this experiment is not known.

Compound	$\chi^2$	Bragg-R factor	R <sub>p</sub>	R <sub>wp</sub>	R <sub>f</sub>
Dy <sub>2</sub> (Ti <sub>0.2</sub> Zr <sub>0.2</sub> Hf <sub>0.2</sub> Ce <sub>0.2</sub> Si <sub>0.2</sub> ) <sub>2</sub> O <sub>7</sub>	1.31	1.53	31.30	12.20	3.20

**Table 4.1:** Table showing all the goodness of fit parameters obtained using Rietveld refinement from the powder XRD.

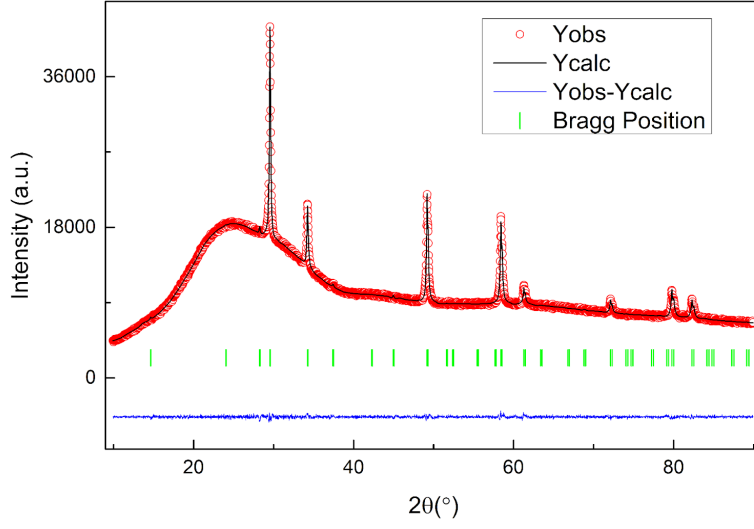


Fig 4.2: Rietveld refinement of the powder X-Ray diffraction pattern.

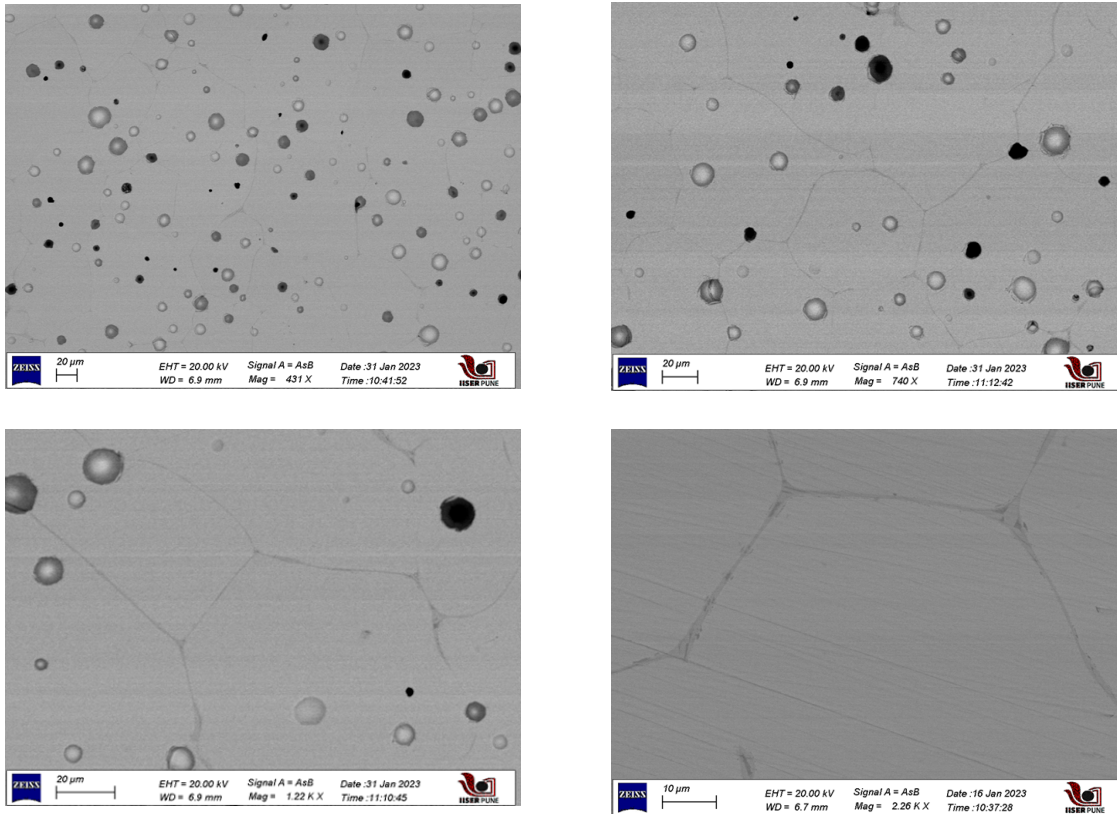
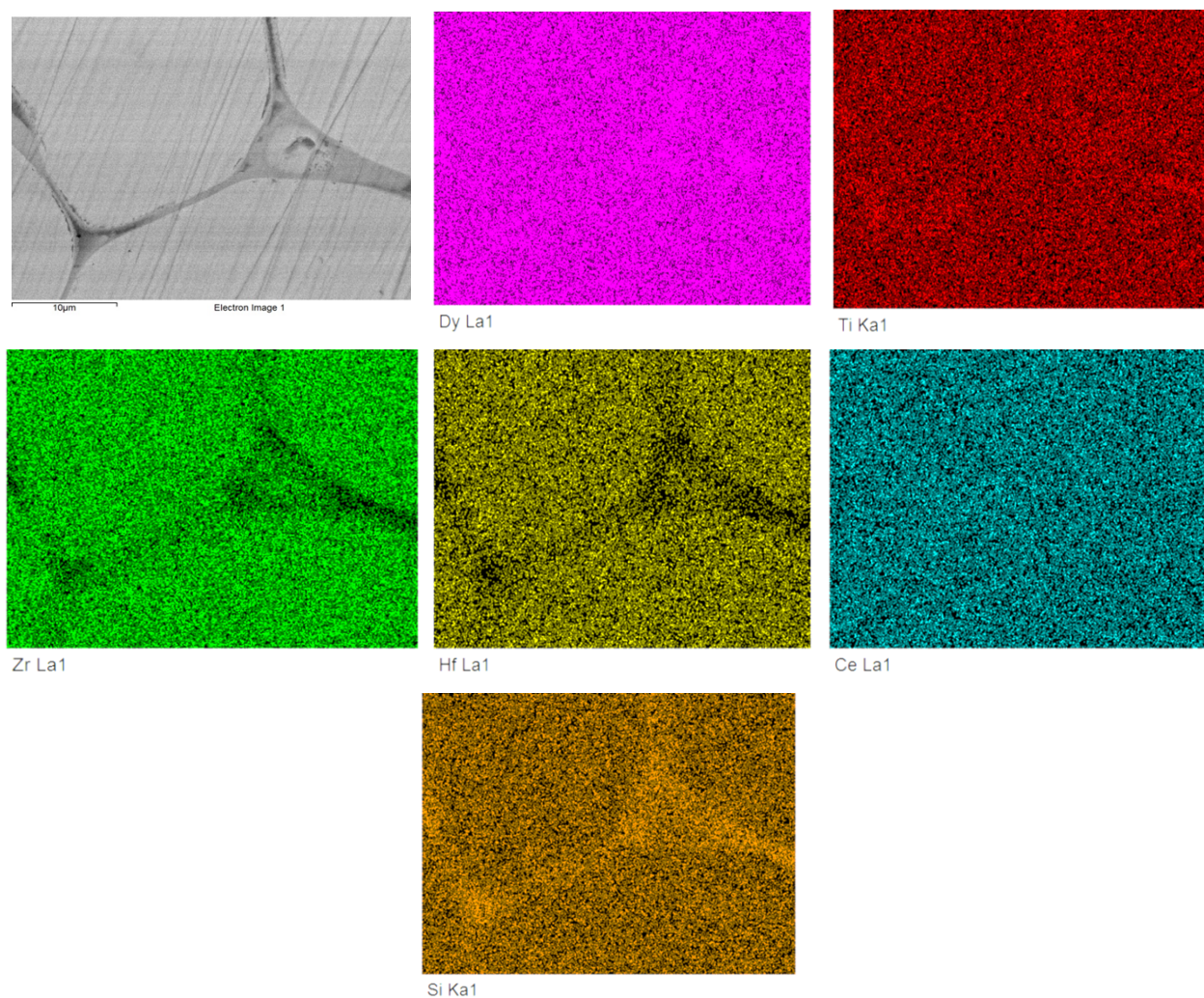


Fig 4.3: Morphology of the sample sintered for 12hr at different magnification scales.

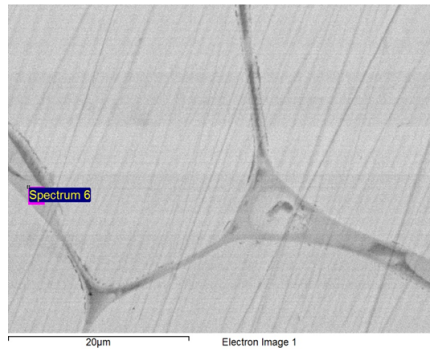


**Fig 4.4:** Shows the elemental mapping of the sample after 12 hr sintering.

While XRD indicates that the sample is pure, a very small quantity of a secondary phase is observed upon examination with scanning electron microscopy (SEM). Further analysis through elemental mapping confirmed the presence of a Si-rich secondary phase, with lower concentrations of Zr and Hf compared to other B-site elements. In contrast, the A-site element Dy was uniformly distributed throughout the sample, as expected.

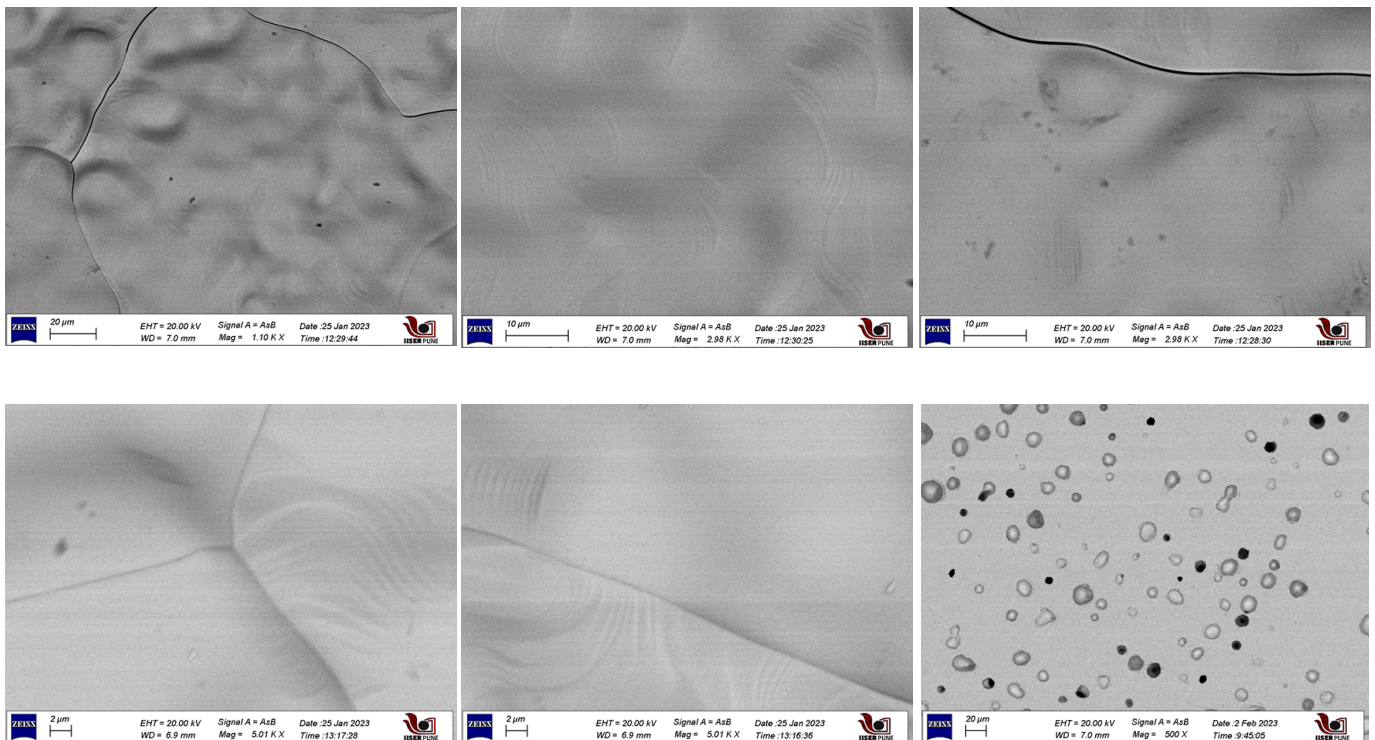


Element	Dy	Ti	Zr	Hf	Ce	Si
Atomic %	44.02	10.44	8.25	6.70	4.70	25.89



**Table 4.2:** This table shows the atomic% of various elements at the point labeled spectrum 6 in the figure shown below.

EDX also shows a higher concentration of Si in the secondary phase.



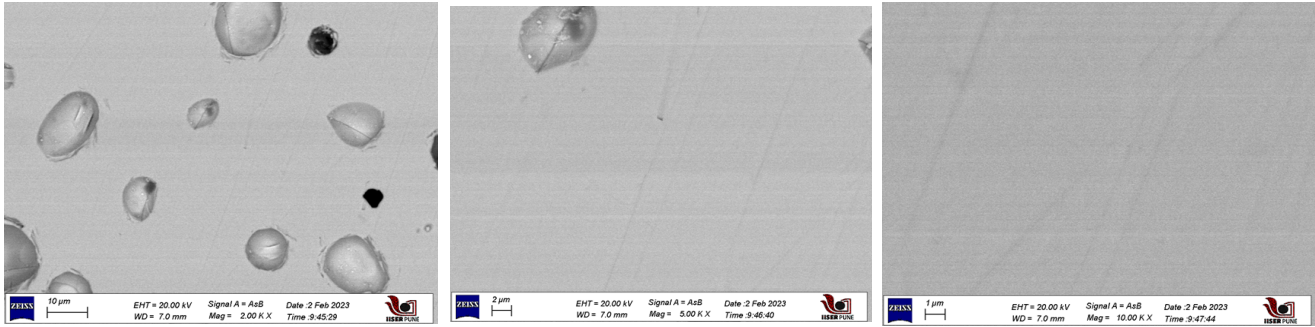


**Fig 4.5:** shows the morphology of the sample after sintering it for 44hr. The first five images show the morphology of the outer surface.

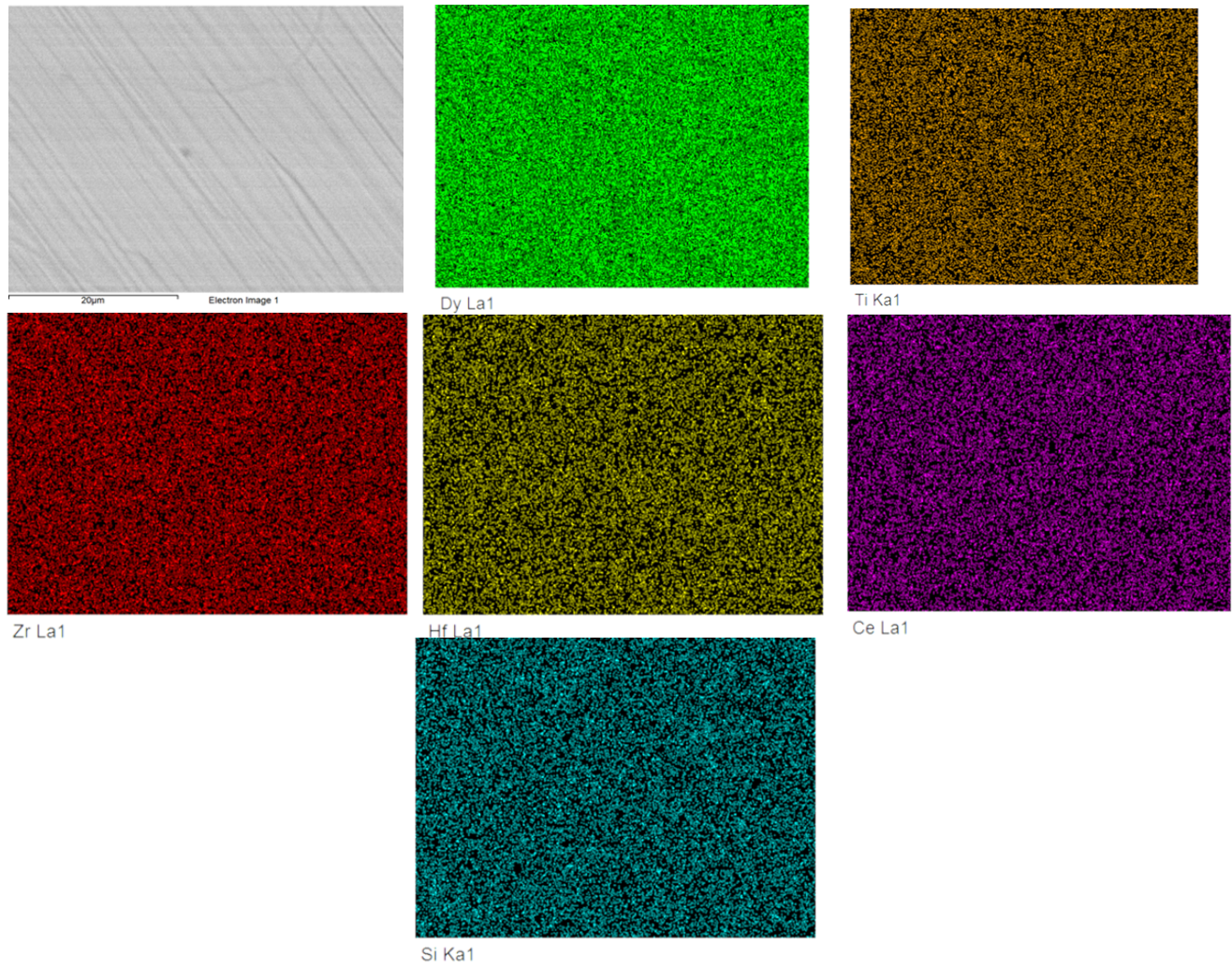


**Fig 4.6:** Elemental mapping of the pure phase  $Dy_2(Ti_{0.2}Zr_{0.2}Hf_{0.2}Ce_{0.2}Si_{0.2})_2O_7$ .

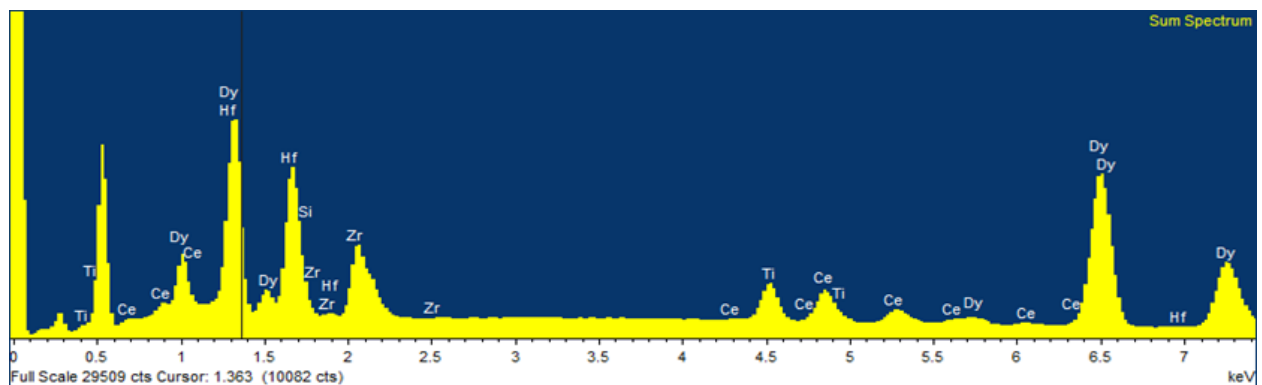


**Fig 4.7:** Energy spectrum of different elements taken over the area shown in Figure 4.6.

Element	Dy	Ti	Zr	Hf	Ce	Si
Atomic %	48.85	8.59	17.02	14.94	6.91	3.70

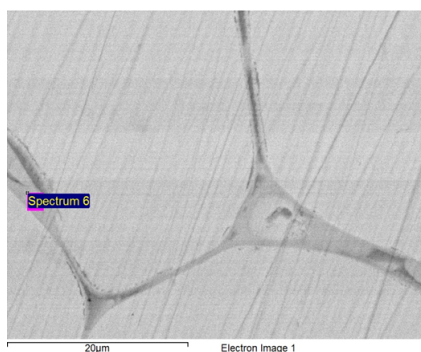


**Table 4.3:** Table shows the atomic % of various elements in the area shown in Figure 4.6.

Both the morphology and elemental mapping analyses provided evidence of the uniform distribution of A and B-site elements, indicating the formation of a pure, single phase. However, the EDX data showed a slight deviation for the B-site element, which we attributed to the possible overlap of energy spectra from different elements.

### 4.3 Thermal Reversibility and high entropy stabilized defect Fluorite

Thermal reversibility is a powerful method to prove entropy-stabilized systems. We did the 10 days of annealing of the pure phase sample at a lower temperature than the sintering temperature which was 1400°C followed by a slow cooling rate of 250°C per hour to see the phase segregation if any.

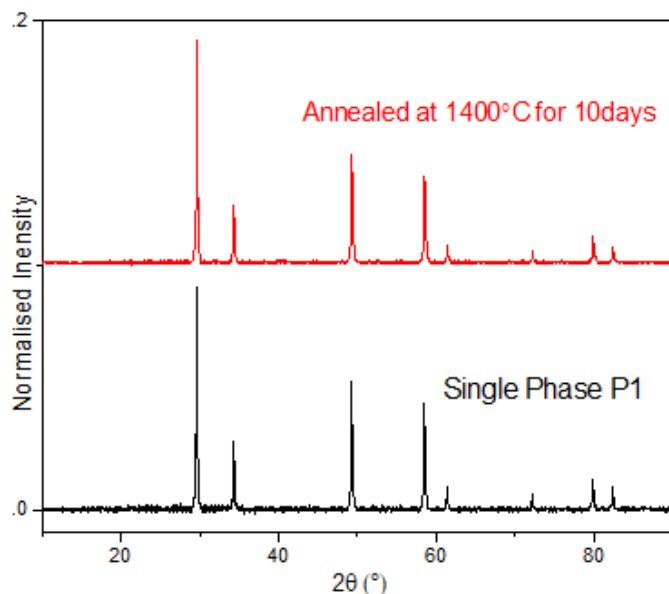


Fig 4.8: Shows the XRD graph of the annealed sample.

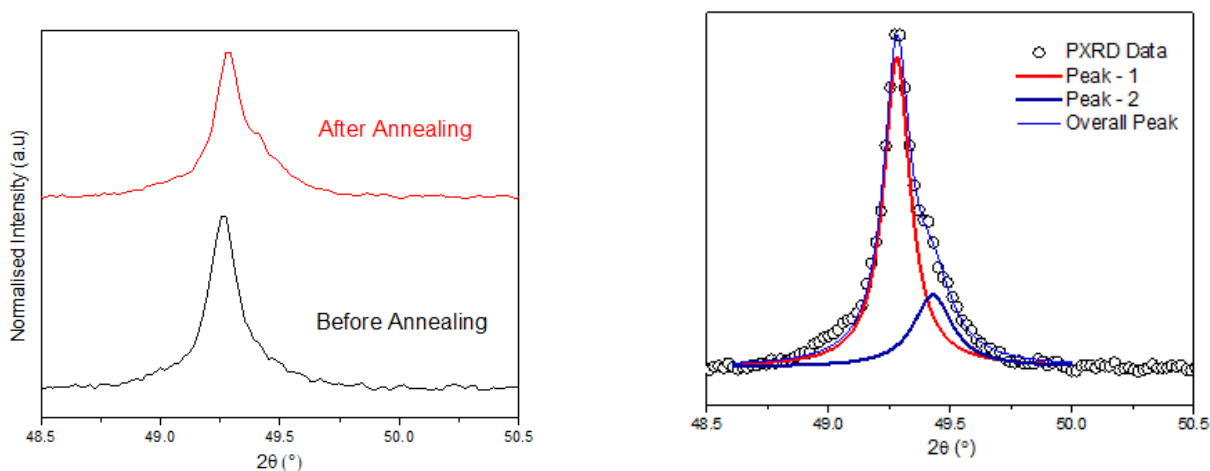


Fig 4.9: (a) Zoomed XRD peak before and after annealing. (b) Gaussian fitting of the peak corresponds to an annealed sample

Based on the XRD analysis, we detected the emergence of a secondary phase, which was best fit analytically with a Gaussian function. This suggests that the stabilization of the pure phase is due to its entropic origin, as expected[17,12]. However, the SEM analysis did not reveal any sign of a secondary phase, which could be because the secondary phase is too small to detect.

#### 4.4 Thermal Conductivity Measurements

High-entropy pyrochlore is a type of high-entropy alloy material that exhibits a remarkably low thermal conductivity. In insulators, thermal transport occurs via lattice vibrations or phonons, and the disorder in high-entropy oxides results in reduced thermal conductivity. For instance,  $(\text{Mg}_{0.2}\text{Co}_{0.2}\text{Ni}_{0.2}\text{Cu}_{0.2}\text{Zn}_{0.2})\text{O}$  has an amorphous-like thermal conductivity of 2.95 W/m/K[22]. This feature makes them suitable for applications that require thermal insulation, such as thermal barrier coatings. While high-entropy pyrochlores have been studied extensively for their properties related to disorder and lattice distortion rather than entropic stabilization, they show promise as candidates for such applications. For example,  $(\text{La}_{0.2}\text{Ce}_{0.2}\text{Nd}_{0.2}\text{Sm}_{0.2}\text{Eu}_{0.2})_2\text{Zr}_2\text{O}_7$  has a thermal conductivity of 0.76 W/m/K at room temperature, which is lower than that of mono-cationic pyrochlores (around 2 W/m/K at room temperature and 1.5 W/m/K at 1000 °C) [23,24,25,26] and also less than the most commercially used material, 8YSZ, which has a thermal conductivity of about 2 W/m/K [27]. A new entropy-stabilized pyrochlore  $\text{Dy}_2(\text{Ti}_{0.2}\text{Zr}_{0.2}\text{Hf}_{0.2}\text{Sn}_{0.2}\text{Ge}_{0.2})_2\text{O}_7$  has been reported with a constant thermal conductivity of around 1.4 W/m/K throughout the temperature[12].

In our study, we measured the thermal conductivity of a pure-phase  $\text{Dy}_2(\text{Ti}_{0.2}\text{Zr}_{0.2}\text{Hf}_{0.2}\text{Ce}_{0.2}\text{Si}_{0.2})_2\text{O}_7$  sample from room temperature up to 873K. Thermal conductivity is corrected using the formula  $\mathbf{K}_{\text{raw}}/\mathbf{k}_{\text{corrected}}=\mathbf{1-(4P/3)}$  [26] to avoid the porosity factor. Measured thermal conductivity shows a constant value around 1.2 W/m/K throughout the temperature which shows a glass-like behavior as expected due to the high degree of disorder present in the system.

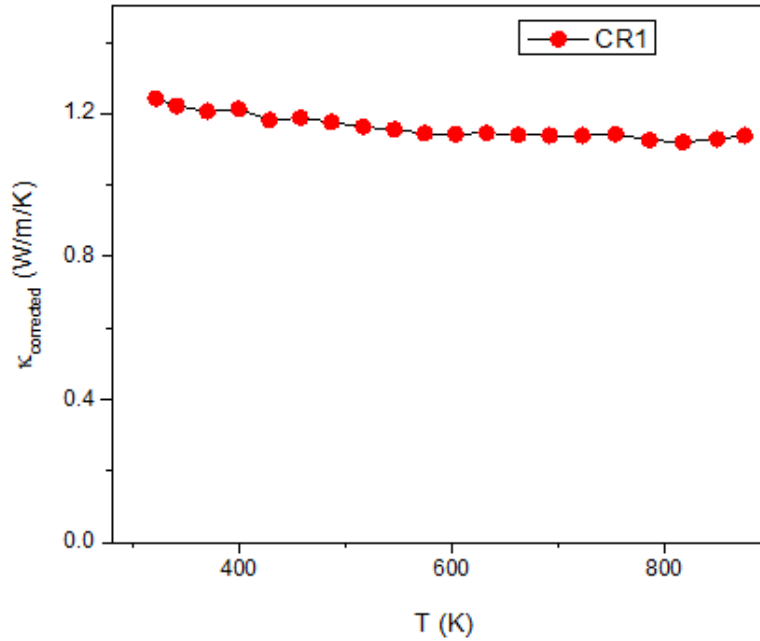


Fig 4.10: Thermal conductivity as measured from room temperature to 873K.

## 4.5 Summary

To summarize, our study has demonstrated the successful synthesis of a pure phase of entropy-stabilized defect fluorite (Fd-3m) using various characterization techniques, including powder XRD, SEM, and EDX. Our measurements of thermal conductivity indicate a glass-like behavior with exceptionally low thermal conductivity. However, there is still much more to be explored regarding the potential applications of this high-entropy material, including its irradiation resistance and potential as a TBC material. The magnetic susceptibility has been explored in  $\text{Dy}_2(\text{Ti}_{0.2}\text{Zr}_{0.2}\text{Hf}_{0.2}\text{Sn}_{0.2}\text{Ge}_{0.2})_2\text{O}_7$  sample and it came out to be paramagnetic in nature due to the dominant nature of  $\text{Dy}^{3+}$  moments [12]. We are yet to measure the magnetic measurement but still hoping for the same behavior due to the very high magnetic moment of the  $\text{Dy}^{3+}$  cation which is around  $10\mu_B$ .

## Chapter 5

### Effect of Bi Substitution in $\text{Eu}_2\text{Ru}_2\text{O}_7$

In this chapter, we will discuss the outcomes of the isovalent substitution of  $\text{Eu}^{3+}$  with  $\text{Bi}^{3+}$  in  $\text{Eu}_2\text{Ru}_2\text{O}_7$ . We examined how the introduction of Bi impacted both the structure and transport properties, and we will elaborate on these findings in the following sections.

#### 5.1 Synthesis and structural characterization

The series  $(\text{Eu}_{1-x}\text{Bi}_x)_2\text{Ru}_2\text{O}_7$  ( $x = 0, 0.02, 0.035, \text{ and } 1$ ) were synthesized in the air using the solid-state synthesis route with precursors  $\text{Eu}_2\text{O}_3$  (Sigma Aldrich 99.9%),  $\text{Bi}_2\text{O}_3$  (Sigma Aldrich 99.9%), and  $\text{RuO}_2$  (Sigma Aldrich 99.9%). The mixture was ground and cold-pressed in a stainless steel die (13mm, 9 tons), and then fired at  $750^\circ\text{C}$  in air. The sintering temperature in the subsequent cycles was gradually increased in small steps up to  $1050^\circ\text{C}$  to prevent the vaporization of volatile  $\text{RuO}_2$ . Before the start of a new sintering cycle, the pellets from the previous cycle were grounded and repelletized. The synthesis process was only considered complete when the powder X-ray diffraction showed the formation of the pyrochlore phase with little no traces of precursor materials. The phase formation was monitored using a Bruker D8 Advance powder X-ray diffractometer.

The results indicated that compositions with higher Bi concentration required lower sintering temperatures to obtain a single phase.  $\text{Bi}_2\text{Ru}_2\text{O}_{6.96}$ , for example, formed easily at around  $900^\circ\text{C}$  for a total sintering duration of approximately 72 hours while for the other three compounds, it took around 126-128 hours. Compositions in the range of  $x=0$  to 0.035 required repeated sintering at higher temperatures. The ease of formation of the pyrochlore phase with increasing Bi substitution was attributed to the high diffusivity of  $\text{Bi}_2\text{O}_3$ , which has a melting temperature of around  $815^\circ\text{C}$  [28].

Throughout the synthesis process, the phase formation of all samples was monitored using a Bruker D8 diffractometer. The powder X-ray diffraction patterns of the entire  $(\text{Eu}_{1-x}\text{Bi}_x)_2\text{Ru}_2\text{O}_7$  series were indexed based on the pyrochlore structure. However, very weak diffraction peaks resulting from unreacted precursors,  $\text{RuO}_2$ , were observed for all samples, as indicated by the asterisk (\*) in Figure 5.1 below.

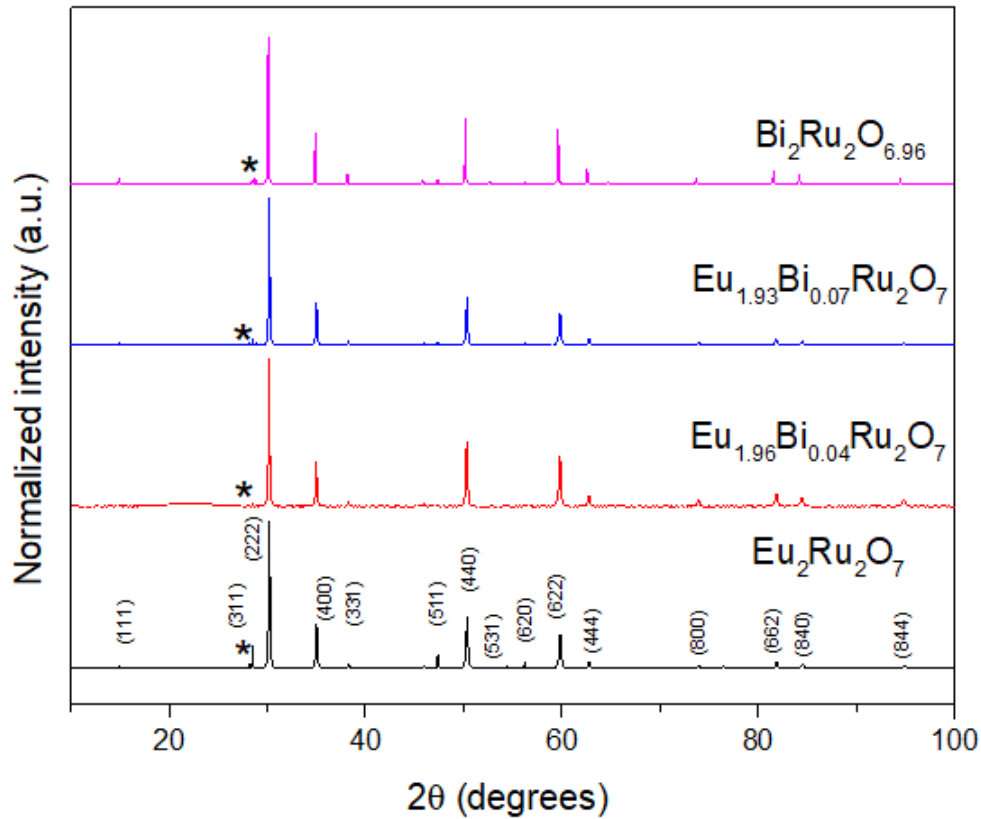


**Fig 5.1:** XRD graph of final compounds with different compositions.

### 5.1.1 Lattice parameter variation in $(\text{Eu}_{1-x}\text{Bi}_x)_2\text{Ru}_2\text{O}_7$

With the introduction of Bi into the material, we anticipated a gradual increase in lattice parameters due to the significantly larger lattice parameters of  $\text{Bi}_2\text{Ru}_2\text{O}_{6.96}$  (BRO) in comparison



to  $\text{Eu}_2\text{Ru}_2\text{O}_7$  (ERO). However, we found that initial Bi-doping in ERO resulted in a small anomalous lattice contraction. As demonstrated by the XRD lines Fig.5.2b, a shift towards higher angles was observed across the  $(\text{Eu}_{1-x}\text{Bi}_x)_2\text{Ru}_2\text{O}_7$  series for x values less than or equal to 0.035, indicating lattice contraction. This lattice parameter variation with x is shown in Fig.5.2a.

Our findings indicate a violation of Vegard's law in this series at lower concentrations. This phenomenon is similar to that observed recently in the Iridates series, as reported by Prachi Telang et al.[29]. However, in the case of the Ru series, the degree of contraction is significantly less when compared to the Ir series.

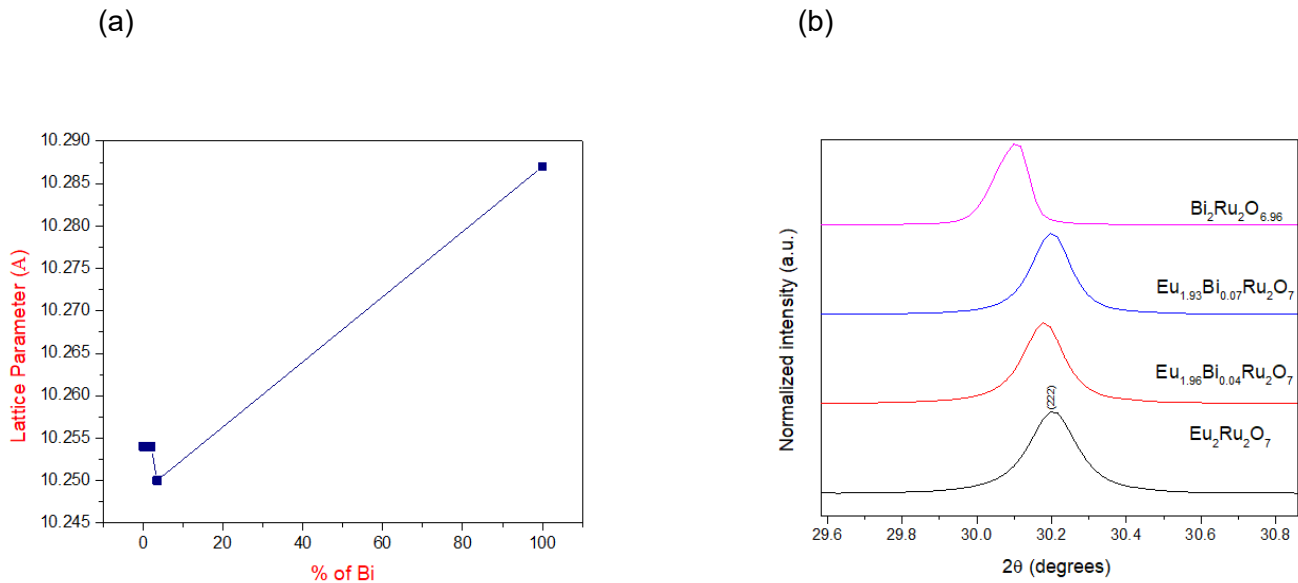


**Fig 5.2:** (a) Variation of lattice parameter with Bi doping in %. (b) zoom view of (222) peak for all compounds.

The morphology of all the samples was examined using SEM. Fig. Below shows the FESEM images for various doping concentrations. As the concentration of Bi increases, the size of the grain size also increases. For compositions near the BRO ( $x = 1$ ), clear octahedral-shaped grains were observed. This increase in crystalline tendency with Bi substitution aligns with the notion that the inclusion of Bi accelerates the formation of the pyrochlore phase. To determine the Eu: Bi ratio, pieces of the pellets were polished for EDX measurements. For the sample with  $x = 0.02$ , the calculated Bi: Eu ratio was 0.020, while the experimental value, averaged over 8 different points, was 0.017, demonstrating good agreement.

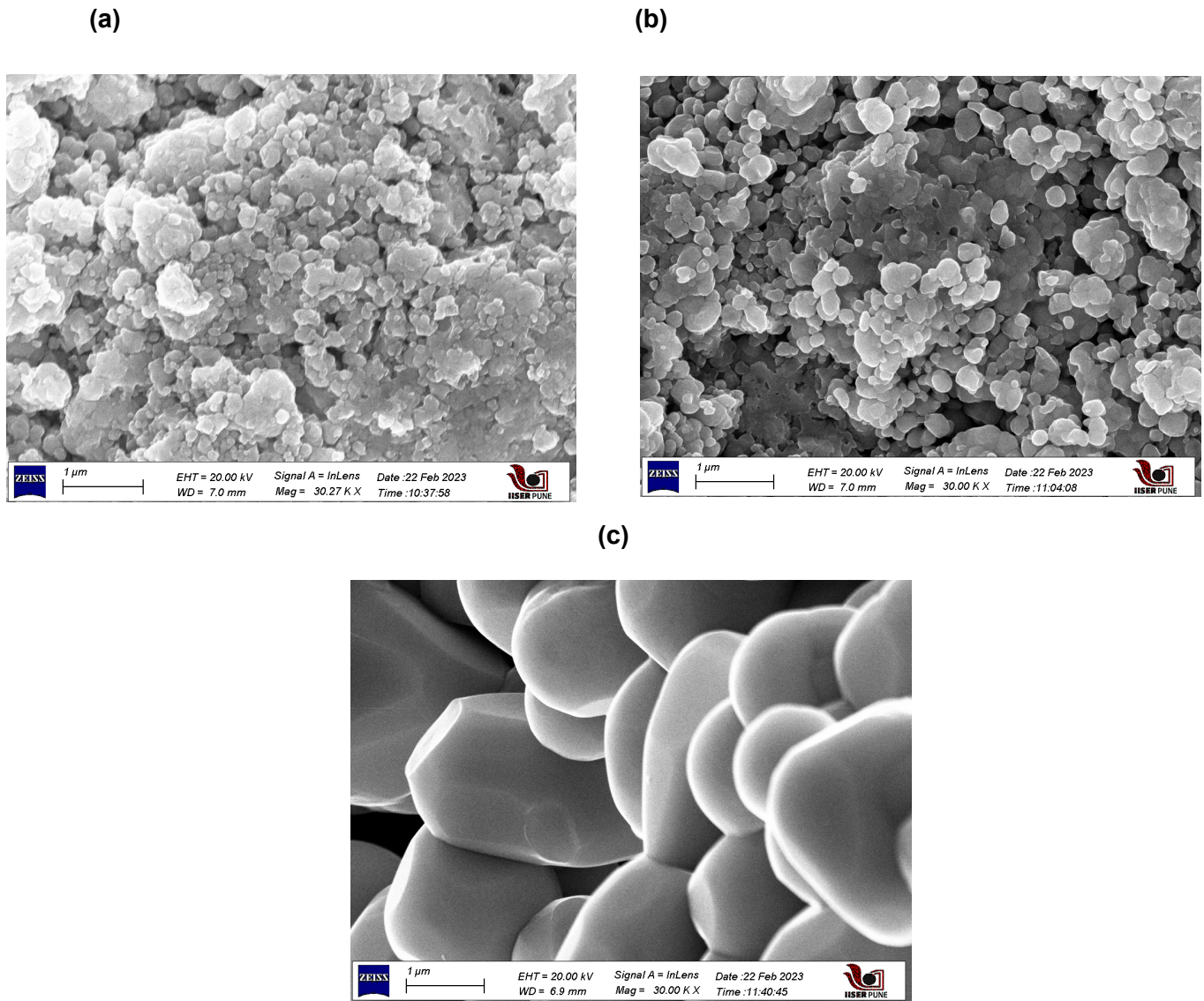


**Fig 5.3:** (a)  $X=0$ , (b)  $X=0.02$ , (c)  $X=1$ , FESEM images. Grain size increases with Bi doping.

## 5.2 Thermoelectric Properties Measurement, Results, and Discussion

We have conducted thermoelectric measurements on the synthesized samples. For the first three samples, we observe that the thermal conductivity initially decreases up to a temperature of

550K. This behavior can be explained by the resistive Umklapp scattering of three phonons[30]. However, beyond 550K, the thermal conductivity increases again, which is not expected unless there is a significant bipolar contribution where presence should also manifest itself in the temperature variation of electrical conductivity and Seebeck coefficient. In the case of  $x= 0.02$ , we observe a reduction in the thermal conductivity, which may be due to lattice disturbances caused by the substitution. For higher doping levels, we again observe an increase in thermal conductivity. This is because, with higher electron doping, the electronic contribution becomes dominant and approaches the behavior of the end compound, which is expected in the metallic case.

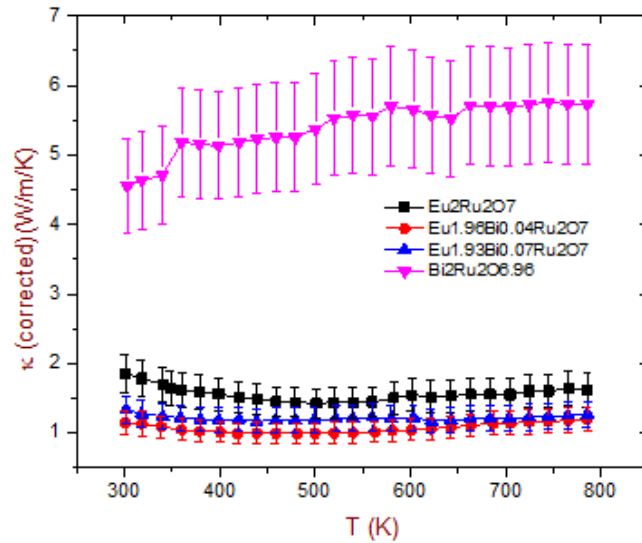


**Fig 5.4:** Corrected thermal conductivity variation with temperature with different  $x$  with 10% of the error bar.

In order to avoid the porosity in the sample we have corrected the thermal conductivity by using the formula  $K_{\text{raw}}/k_{\text{corrected}}=1-(4p/3)$  where 'p' is the porosity of the sample given by  $p = 1-\rho_r$  [where  $\rho_r$  is the relative density of the sample[26]]. The calculated density for the different samples were 4.8389, 4.4424, 4.9797, and 7.30 in g/cc respectively for  $x = 0$ , 0.02, 0.035, and  $x = 1$ .

The high-temperature electrical conductivity measurement is also shown in figure 5.5 below. It shows semiconducting nature for  $x = 0$ , 0.02, and 0.035 (i.e;  $d\sigma/dT>0$ ) while for the  $x = 1$  sample  $\sigma$  increases up to 400K and a decreasing trend thereafter.

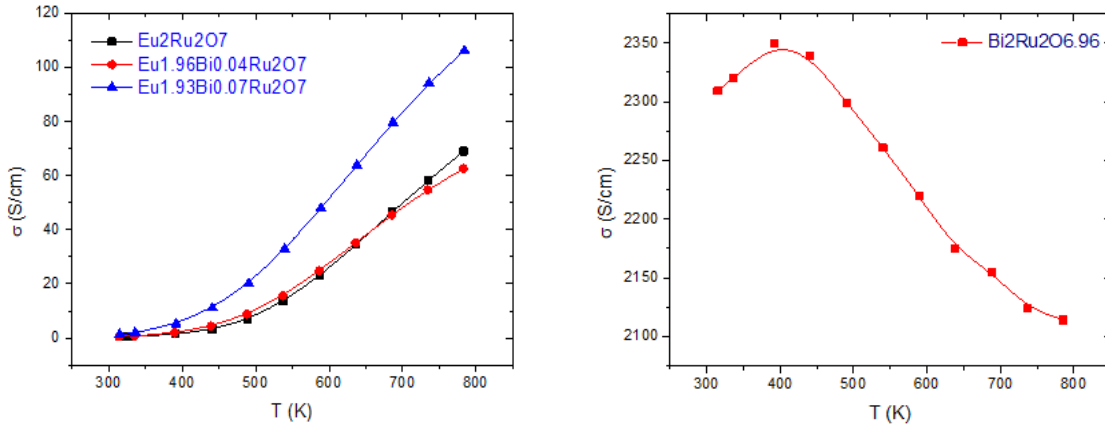


**Fig 5.5:** Shows the variation of electrical conductivity for all samples.

The figure below shows the measured thermopower for all the samples. In the case of  $\text{Eu}_2\text{Ru}_2\text{O}_7$ , the thermopower remains positive for all temperatures, indicating that the dominant charge carriers are hole-like. While for  $\text{Bi}_2\text{Ru}_2\text{O}_7$ , the thermopower is not only negative, but it also exhibits typical metal-like behavior where the absolute value of  $S$  increases with increasing temperature. This qualitative behavior and sign of  $S$  are consistent with previous reports on ruthenate pyrochlore [30,31]. Based on the variation of  $S$  with  $x$ , we can infer that  $x = 0.02$  and  $0.035$  samples exhibit a p-n-p transition, while the  $x = 1$  sample shows an n-p transition upon heating.

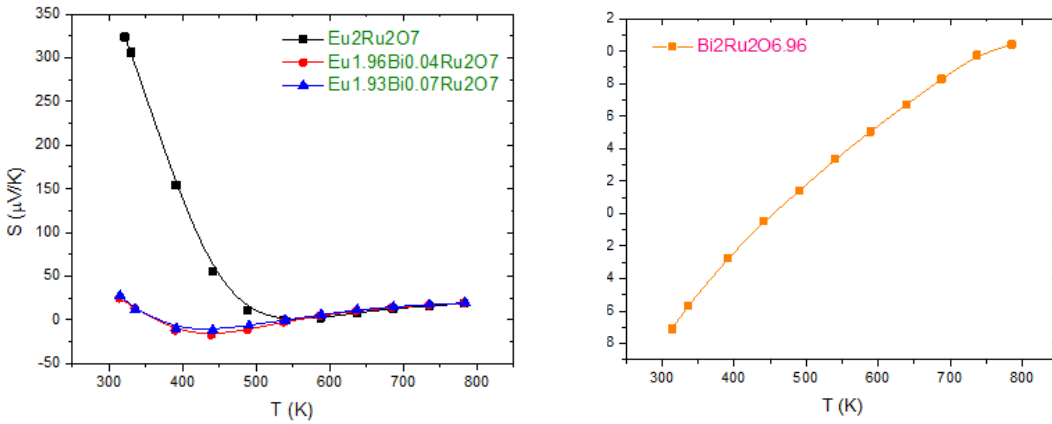
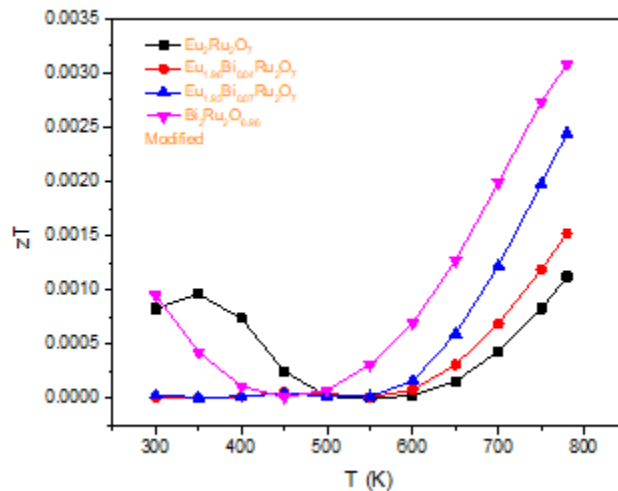


**Fig 5.6:** Variation of thermopower  $S$  with temperature for different  $x$ .

Calculated zT values are shown below in the graph. zT values are calculated using the formula Given in equation (a) below[30]. where terms have their usual meaning.

$$zT = \frac{S^2 \sigma}{k} T \dots\dots\dots (a)$$

Thermoelectric materials such as Bi<sub>2</sub>Te<sub>3</sub>, PbTe, and Si-Ge alloys have been traditionally used for temperature ranges of 200°C, 400-600°C, and 400-1000°C, respectively. However, these materials face limitations like poor durability in air, high cost of comprising elements, low abundance, and high toxicity, making them difficult to use commercially. Oxide-based thermoelectric materials have gained attention in recent decades due to their lack of these drawbacks[32].



5.7: Variation of zT with temperature for all compounds.

Examples of promising oxide thermoelectric materials include CaMnO<sub>3</sub>-based perovskites, Al-doped ZnO, layered cobalt oxides such as NaCo<sub>2</sub>O<sub>4</sub> and Ca<sub>3</sub>Co<sub>4</sub>O<sub>9</sub>, and SrTiO<sub>3</sub>-related phases. Among these, In<sub>2</sub>O<sub>3</sub>-SnO<sub>2</sub> complex oxides demonstrate the highest power factor of 1.6 x 10<sup>-4</sup> W m<sup>-1</sup> K<sup>-2</sup> and a zT value of 0.06 at 1000°C[33]. Additionally, zT values of 0.45 at 1273 K have

been reported for  $\text{In}_{1.8}\text{Ge}_{0.2}\text{O}_3$ , [34] and the composition  $\text{Zn}_{0.96}\text{Al}_{0.02}\text{Ga}_{0.02}\text{O}$  shows the highest zT of around 0.65 at 1273K[35]. Furthermore, recent studies show that a zT value of around 2.4 can be achieved with a two-dimensional electron gas (2-DEG) formed at the interfaces of a superlattice structure made by  $\text{SrTiO}_3$  epitaxial thin films[36].

In our case, the zT values vary from 0 to 0.004 for the  $x = 0, 0.02, 0.035,$  and 1 compounds, and a maximum zT value is observed for  $\text{Bi}_2\text{Ru}_2\text{O}_{6.96}$  which is around 0.003 at 800K. If we compare the thermoelectric figure of merit of the pyrochlore oxides reported [30,31] and synthesized are very low compared to the current oxides which are reported and hence it requires more investigation or strategies to increase the overall thermoelectric performance of these oxides.

# Chapter 6

## Summary and Outlook

This thesis contains two projects one is High entropy pyrochlore and the other is ruthenates-based pyrochlore. The first part of this thesis, i.e chapter-3, chapter-4 (also in appendix-A) contains a study of a new Si-based high entropy defect fluorite which includes synthesis, characterization, and thermal conductivity measurement. Although some other measurements like irradiation resistance are yet to be done. As of now, we have successfully synthesized the two HEP  $\text{Dy}_2(\text{Ti}_{0.2}\text{Zr}_{0.2}\text{Hf}_{0.2}\text{Ce}_{0.2}\text{Si}_{0.2})_2\text{O}_7$  and  $\text{Dy}_2(\text{Ti}_{0.25}\text{Zr}_{0.25}\text{Hf}_{0.25}\text{Si}_{0.25})_2\text{O}_7$ . Both XRD and SEM analyses confirmed the presence of a pure defect fluorite phase crystallized in the Fd-3m space group, with a slight loss of  $\text{CeO}_2$  observed during the longer sintering period.  $\text{Dy}_2\text{Si}_2\text{O}_7$  does not stabilize in the cubic phase even at high temperatures and pressure[1]. We incorporate 20% of Si at the B site with a stable cubic phase. Also, the thermal reversibility mechanism confirms the entropic origin of its stabilization. The measured thermal conductivity of both compounds is less than 1 W/m/K across the temperature range of 300K to 873K, which is almost 50-60 % less than that of commercially used 8YSZ [27]. We observed a constant thermal conductivity (almost) which could be due to the high degree of disorder introduced in the system in terms of their mass and cationic radius. The same nature of thermal conductivity was also observed in  $\text{Dy}_2(\text{Ti}_{0.2}\text{Zr}_{0.2}\text{Hf}_{0.2}\text{Sn}_{0.2}\text{Ge}_{0.2})_2\text{O}_7$  compounds by Pascanut Decorse et al. [12].

The high-temperature stability, ultra-low thermal conductivity, and high irradiation resistance make them potential candidates for thermal barrier coating and nuclear waste management material respectively.

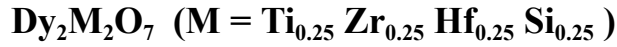
The second part of this thesis consists of a study of the synthesis, characterization, and thermoelectric properties measurement of the  $(\text{Eu}_{1-x}\text{Bi}_x)_2\text{Ru}_2\text{O}_7$  series with  $x = 0, 0.02, 0.035$  and 1. The thermoelectric properties of ceramics are influenced by their chemical composition and crystal structure. Various structural features, such as vacancies, impurities, lone pair electrons, lattice site occupancy, and substitutions, play a crucial role in determining the transport mechanisms of heat and electricity. These structural elements can alter or determine the

scattering mechanisms that impact the thermoelectric behavior of the material. The thermal conductivity shows a glass-like behavior as expected and also the same was reported in the case of other ruthenate pyrochlore for example in the case of  $\text{Pb}_2\text{Ru}_2\text{O}_{6.5}$  thermal conductivity shows the glass-like behavior [30]. In our case overall the maximum  $zT$  observed was 0.003 at 800K for the  $\text{Bi}_2\text{Ru}_2\text{O}_{6.96}$  sample.

The ongoing work includes an attempt to single crystal growth of  $\text{Dy}_2(\text{Ti}_{0.2}\text{Zr}_{0.2}\text{Hf}_{0.2}\text{Ce}_{0.2}\text{Si}_{0.2})_2\text{O}_7$  high entropy defect pyrochlore synthesization of Nd-based high entropy pyrochlore to see how the spin ice low-temperature ground state is varying due to high degree of disorder introduced at B-site.



## Appendix A



### A.1 Synthesis and Characterization

We performed a series of steps to prepare the samples. Initially, we thoroughly mixed the necessary precursors by hand-grinding for 90 minutes. We then subjected the resulting mixture to three rounds of sintering at 1200°C, 1400°C, and 1500°C, respectively. During the sintering process, we pelletized and hand-ground the mixture between each step. Following the third sintering process, we created rods with a diameter of 6mm and a length of a few centimeters. To ensure the rods were dense enough, we further sintered them at 1500°C for approximately 24 hours before transferring them to the image furnace.

In the image furnace, we hung the rods at the convergence point of the lamp power, rotating them at a rate of 4-6 rpm. The sintering process was conducted at 65% power for around 16 hours, followed by air-quenching.

Upon examination with SEM, we observed the presence of secondary phases of Si in the samples. To address this, we increased the sintering time to approximately 48 hours.

XRD analysis confirmed the existence of a single defect fluorite phase, but SEM imaging revealed a second phase containing Si, which was confirmed by EDX analysis in different areas. The figure below shows the XRD pattern after each treatment, along with SEM imaging, mapping, and EDX analysis.

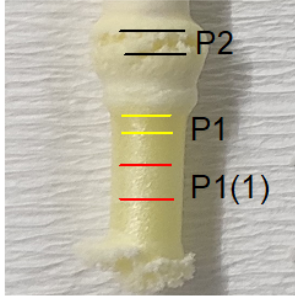
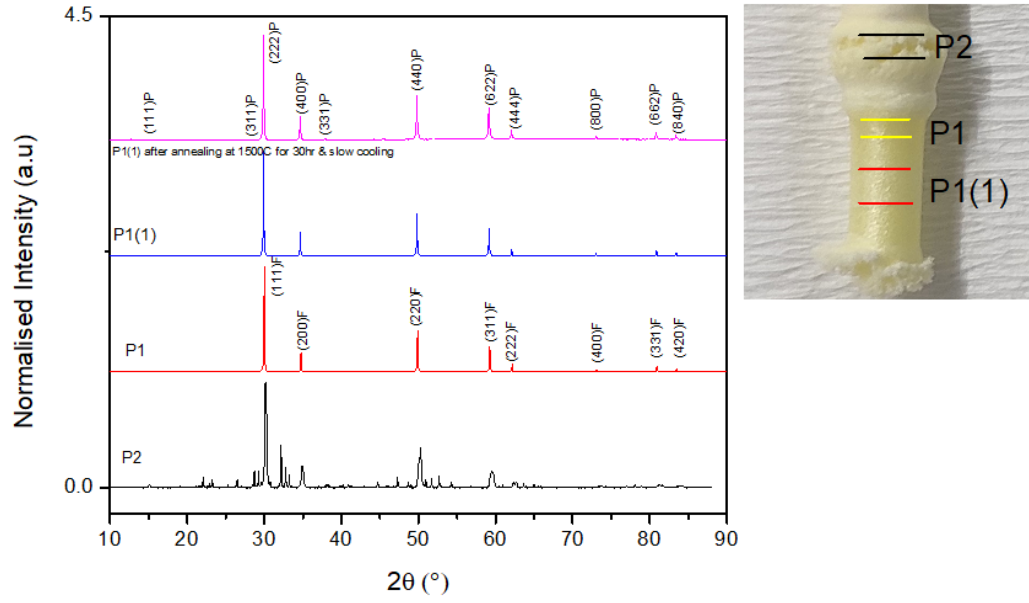
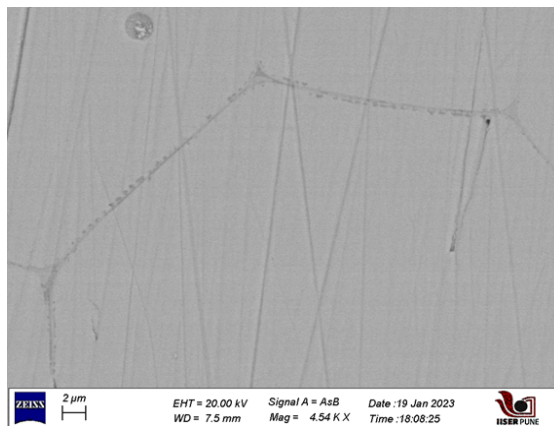
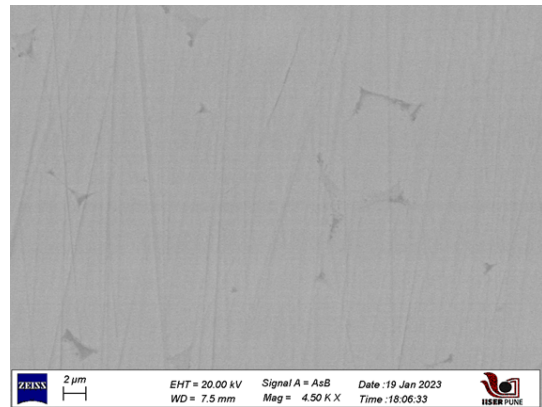
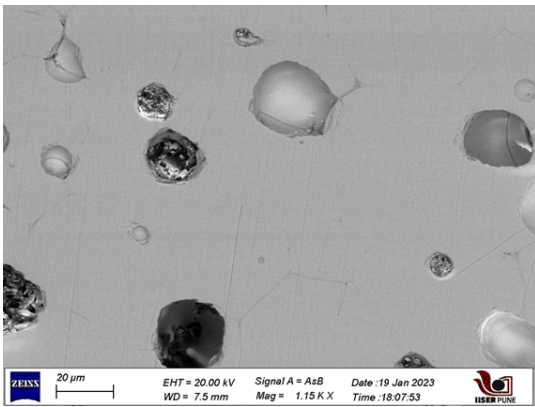
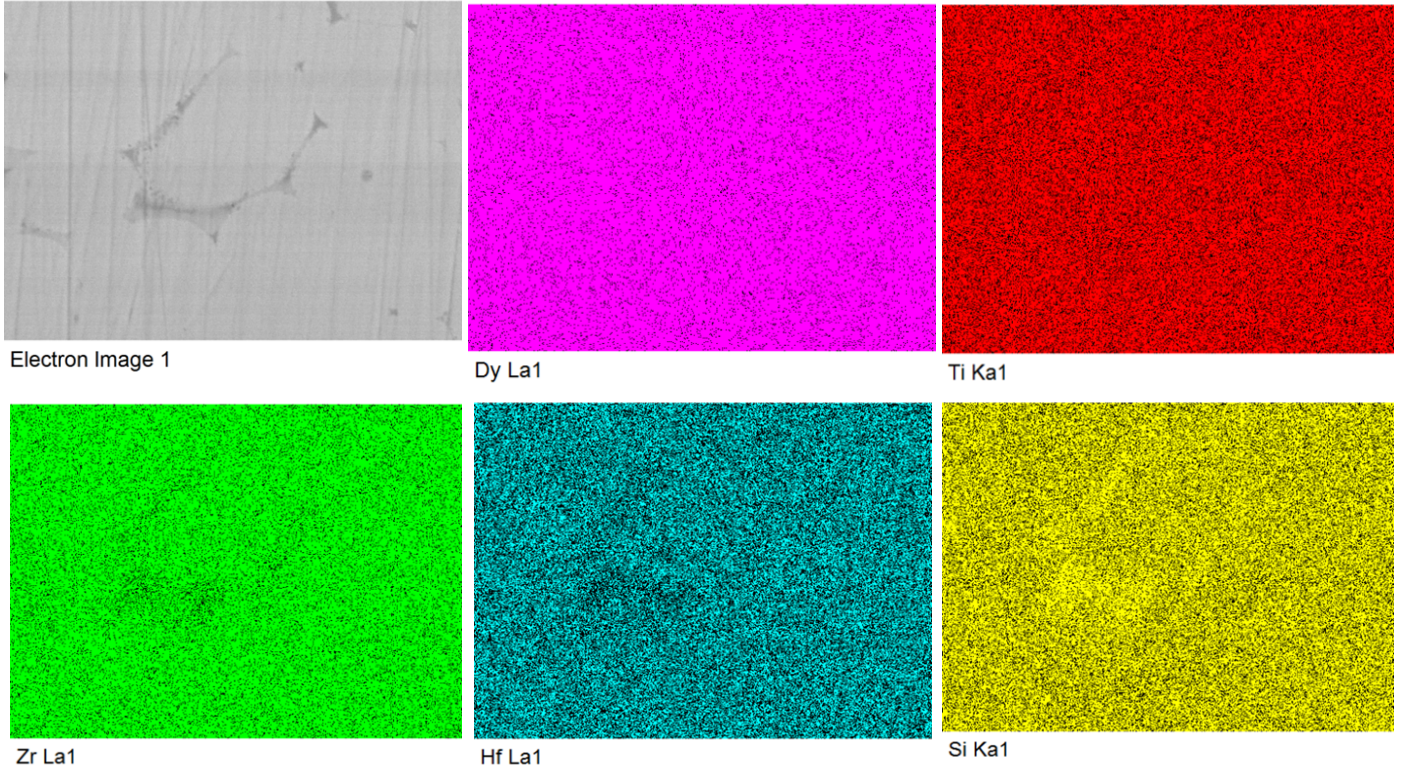


Fig A.1: Powder XRD after 16hr of sintering.

(a)

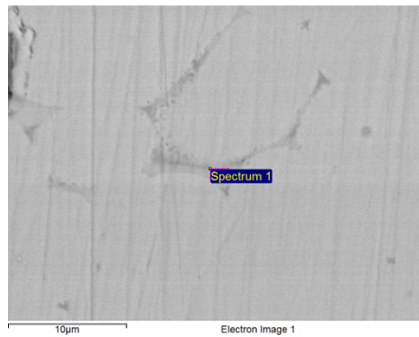


(b)



(c)

Element	Dy	Ti	Zr	Hf	Si
Atomic %	39.71	14.28	20.70	9.27	16.04



Element	Dy	Ti	Zr	Hf	Si
Atomic %	40.15	15.71	27.16	15.56	1.41

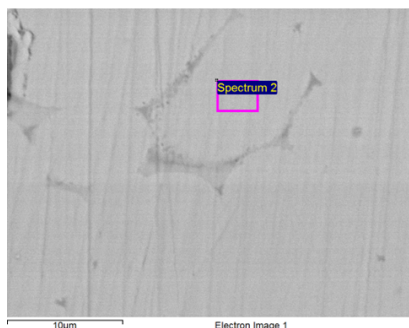


**Fig A.2:** (a) Morphology of the sample at different magnification (b) Elemental mapping (c) EDX at a different area and atomic % of the various element over the same area shown in the table on the right.

SEM analysis confirmed the existence of a secondary phase rich in Si, which was not observed in XRD analysis. This could be attributed to the small amount of the second phase present. Additionally, EDX analysis confirmed the presence of the Si-rich secondary phase.

To address this issue, we increased the sintering time to approximately 48 hours to obtain a single phase, as expected in the case of  $\text{Dy}_2(\text{Ti}_{0.2}\text{Zr}_{0.2}\text{Hf}_{0.2}\text{Ce}_{0.2}\text{Si}_{0.2})_2\text{O}_7$ . The samples were then air-quenched after the sintering process.

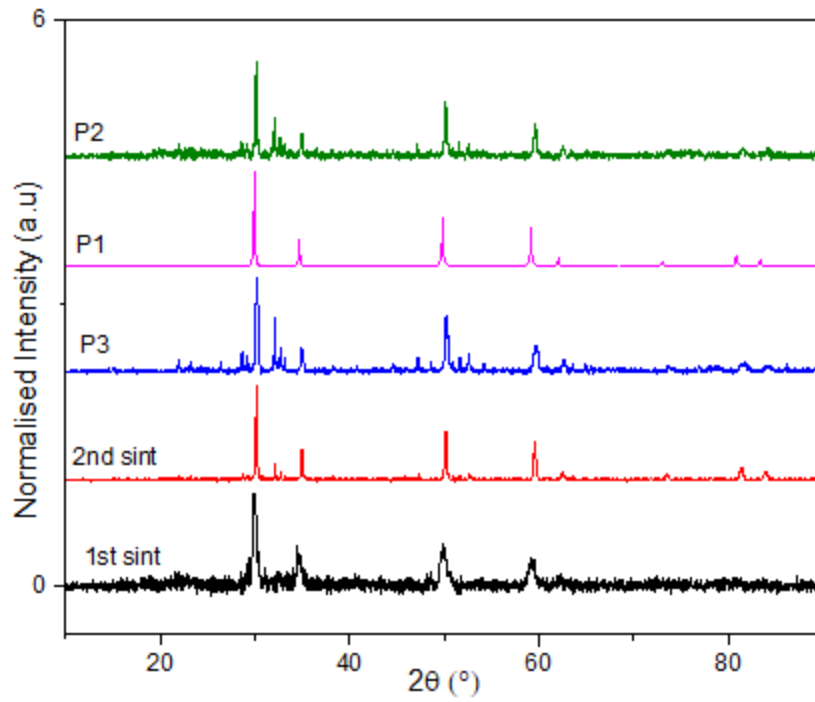
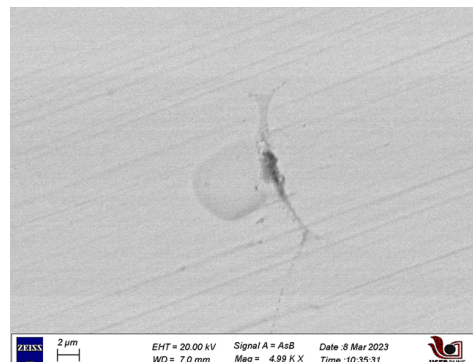
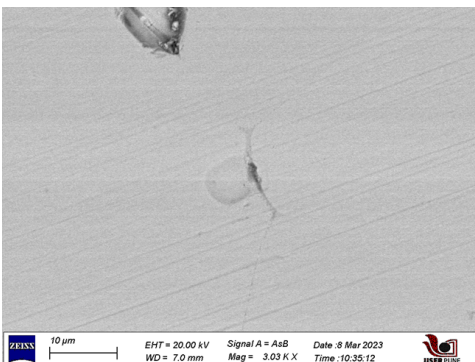
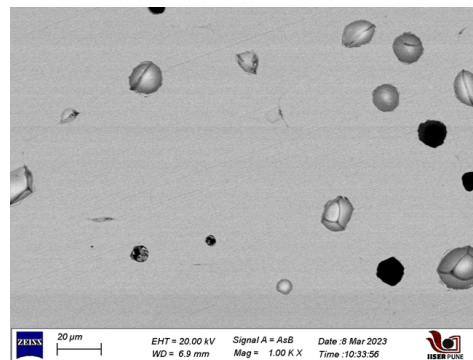
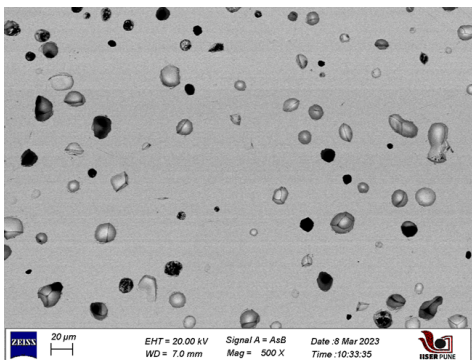
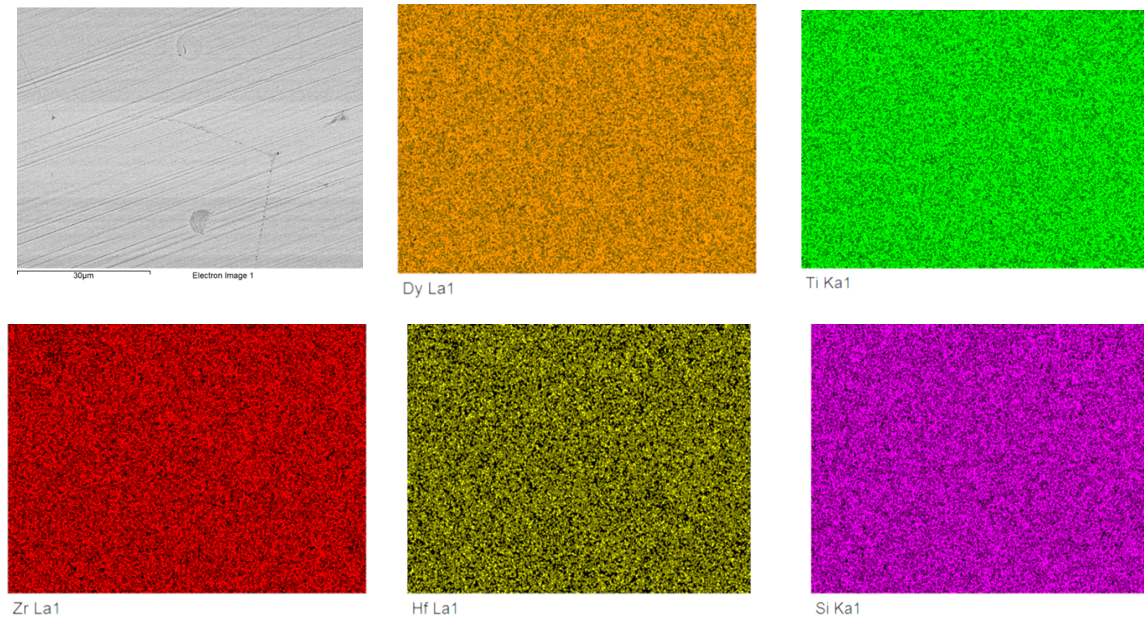


Fig A.3: Powder XRD after 48hrs of sintering.

(a)



(b)



**Fig A.4:** (a) Morphology at different magnification scales (b) Elemental mapping.

## A.2 Results and Summary

XRD analysis confirms the presence of a single defect fluorite phase, but at higher magnification scales, morphology analysis reveals small traces of secondary phases. However, elemental mapping analysis shows a uniform distribution of elements and does not predict the presence of the second phase which can be due to a very small amount of secondary phase.

We employed the LFA technique to measure the thermal conductivity of the sample from room temperature to 873K. The plot of thermal conductivity against temperature indicates a constant value of approximately 0.9 W/m/K across the entire temperature range.

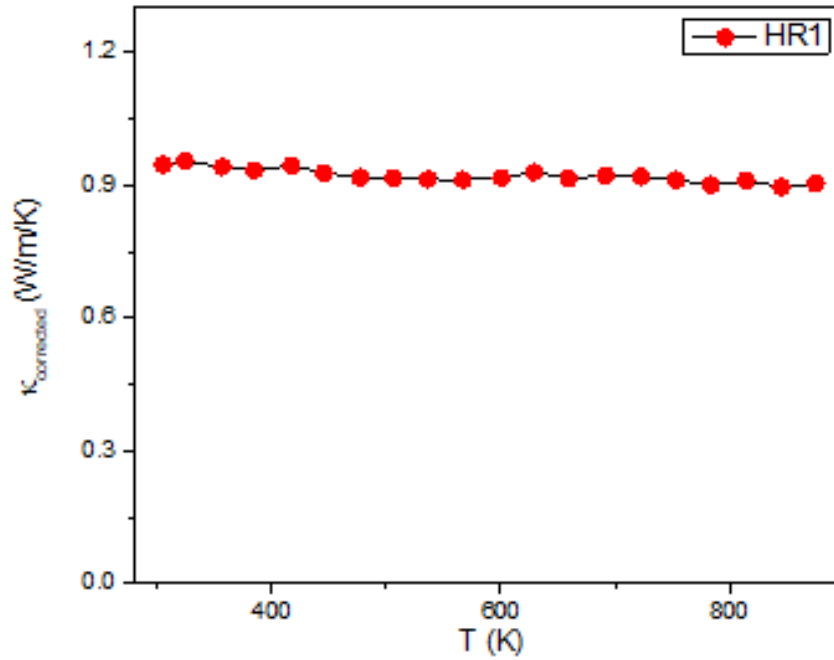


**Fig A.5** Temperature-dependent on thermal conductivity.

In conclusion, increasing the sintering time enabled us to fine-tune the phase formation dynamics through the diffusion mechanism, resulting in the formation of a nearly single phase. It is noteworthy that the configurational entropy in  $\text{Dy}_2(\text{Ti}_{0.2}\text{Zr}_{0.2}\text{Hf}_{0.2}\text{Si}_{0.2})_2\text{O}_7$  is less than that in  $\text{Dy}_2(\text{Ti}_{0.2}\text{Zr}_{0.2}\text{Hf}_{0.2}\text{Ce}_{0.2}\text{Si}_{0.2})_2\text{O}_7$ , which may imply that the former requires higher temperature or entropy to form completely.

## Bibliography

- [1] Subramanian, M. A., G. Aravamudan, and GV Subba Rao. "Oxide pyrochlores—a review." *Progress in Solid State Chemistry* 15.2 (1983): 55-143.
- [2] Gardner, Jason S., Michel JP Gingras, and John E. Greedan. "Magnetic pyrochlore oxides." *Reviews of Modern Physics* 82.1 (2010): 53.
- [3] Telang, Prachi, Kshiti Mishra, and Surjeet Singh. "Tuning the ground state of a candidate Weyl semimetal  $\text{Eu}_2\text{Ir}_2\text{O}_7$  by Bi doping." *APS March Meeting Abstracts*. Vol. 2019. 2019.
- [4] Image is taken from Design Principles for oxide thermoelectric Materials a thesis submitted by Michael W Gaultois.
- [5] Cationic radii are taken from the Shannon.
- [6] Wang, Hao, Changzu Zhu, Zezhen Wang, Menghui Wang, and Yuhong Li. "Mechanical property and irradiation resistance of high entropy pyrochlore ( $\text{Sm}_{0.2}\text{Eu}_{0.2}\text{Gd}_{0.2}\text{Y}_{0.2}\text{Lu}_{0.2}$ )  $2\text{Ti}_2\text{O}_7$ ." *Nuclear Instruments and Methods in Physics Research Section B: Beam Interactions with Materials and Atoms* 533 (2022): 17-22.
- [7] Liu, Chenguang, Qing Peng, Tan Shi, Fei Gao, and Yuhong Li. "Physical properties and radiation tolerance of high-entropy pyrochlores  $\text{Gd}_2(\text{Ti}_{0.25}\text{Zr}_{0.25}\text{Sn}_{0.25}\text{Hf}_{0.25})_2\text{O}_7$  and individual pyrochlores  $\text{Gd}_2\text{X}_2\text{O}_7$  (X= Ti, Zr, Sn, Hf) from first principles calculations." *Scripta Materialia* 220 (2022): 114898.
- [8] Yang, Pan, Yulong An, Dongyan Yang, Yuhong Li, and Jianmin Chen. "Structure, thermal properties and hot corrosion behaviors of  $\text{Gd}_2\text{Hf}_2\text{O}_7$  as a potential thermal barrier coating material." *Ceramics International* 46, no. 13 (2020): 21367-21377.



- [9] Teng, Zhen, Yongqiang Tan, Sifan Zeng, Yan Meng, Chen Chen, Xiaochun Han, and Haibin Zhang. "Preparation and phase evolution of high-entropy oxides  $A_2B_2O_7$  with multiple elements at A and B sites." *Journal of the European Ceramic Society* 41, no. 6 (2021): 3614-3620.
- [10] Wright, Andrew J., Qingyang Wang, Shu-Ting Ko, Ka Man Chung, Renkun Chen, and Jian Luo. "Size disorder as a descriptor for predicting reduced thermal conductivity in medium-and high-entropy pyrochlore oxides." *Scripta Materialia* 181 (2020): 76-81.
- [11] Matsuhira K, Hinatsu Y, Sakakibara T. Novel dynamical magnetic properties in the spin ice compound  $Dy_2Ti_2O_7$ . *Journal of Physics: Condensed Matter*. 2001 Jul 19;13(31):L737.
- [12] Vayer, Florianne, Claudia Decorse, David Berardan, and Nita Dragoie. "New entropy-stabilized oxide with pyrochlore structure:  $Dy_2(Ti_{0.2}Zr_{0.2}Hf_{0.2}Ge_{0.2}Sn_{0.2})_2O_7$ ." *Journal of Alloys and Compounds* 883 (2021): 160773.
- [13] W. Witczak-Krempa, G. Chen, Y. B. Kim, and L. Balents, "Correlated Quantum Phenomena in the Strong Spin-Orbit Regime," *Annu. Rev. Condens. Matter Phys.*, vol. 5, pp. 57–82, 2014.
- [14] Magnetism by Stephen Blundell.
- [15] J. Snyder, J. S. Slusky, R. J. Cava, and P. Schiffer, "How 'spin ice' freezes," *Nature*, vol. 413, no. 6851, pp. 48–51, 2001.
- [16] Brahlek, Matthew, Maria Gazda, Veerle Keppens, Alessandro R. Mazza, Scott J. McCormack, Aleksandra Mielewczyk-Gryń, Brianna Musico et al. "What is in a name: Defining "high entropy" oxides." *APL Materials* 10, no. 11 (2022): 110902.
- [17] Rost, Christina M., Edward Sachet, Trent Borman, Ali Moballegh, Elizabeth C. Dickey, Dong Hou, Jacob L. Jones, Stefano Curtarolo, and Jon-Paul Maria. "Entropy-stabilized oxides." *Nature communications* 6, no. 1 (2015): 8485.

[18] Image is taken from Tuning the ground state of pyrochlore oxides using chemical pressure a thesis submitted by Prachi Telang.

[19] The image has been taken from the thesis Study of half Heusler and related structures as high-temperature thermoelectrics submitted by Kumar Saurabh

[20] <https://www.jeol.co.jp/en/science/em.html>. Jem 2200fs.

[21] <https://www.linseis.com/wp-content/uploads/2020/09/Linseis-Thermal-Conductivity-Tester-v4.pdf>. Linseis. LFA-1000-

[22] J.L. Braun, C.M. Rost, M. Lim, A. Giri, D.H. Olson, G.N. Kotsonis, G. Stan, D.W. Brenner, J.-P. Maria, P.E. Hopkins, Charge-induced disorder controls the thermal conductivity of entropy-stabilized oxides, *Adv. Mater.* 30 (2018) 1805004.

[23] Z. Zhao, H. Xiang, F.-Z. Dai, Z. Peng, Y. Zhou,  $(\text{La}_{0.2}\text{Ce}_{0.2}\text{Nd}_{0.2}\text{Sm}_{0.2}\text{Eu}_{0.2})_2\text{Zr}_2\text{O}_7$ : a novel high-entropy ceramic with low thermal conductivity and sluggish grain growth rate, *J. Mater. Sci. Technol.* 35 (2019) 2647–2651.

[24] Zhang, Yonghe, Min Xie, Fen Zhou, Xiangzhong Cui, Xingeng Lei, Xiwen Song, and Shengli An. "Low thermal conductivity in  $\text{La}_2\text{Zr}_2\text{O}_7$  pyrochlore with A-site partially substituted with equimolar  $\text{Yb}_2\text{O}_3$  and  $\text{Er}_2\text{O}_3$ ." *Ceramics International* 40, no. 7 (2014): 9151-9157.

[25] Liang, Panpan, Shujuan Dong, Jinyan Zeng, Jieyan Yuan, Jianing Jiang, Longhui Deng, Xin Zhou, and Xueqiang Cao. " $\text{La}_2\text{Hf}_2\text{O}_7$  ceramics as potential top-coat materials for thermal/environmental barrier coatings." *Ceramics International* 45, no. 17 (2019): 22432-22436.

[26] Tachibana, Makoto, Ahmad Rifqi Muchtar, and Takao Mori. "Thermal conductivity of rare-earth titanate pyrochlores." *Physical Review Materials* 6, no. 4 (2022): 045405.

[27] M. Zhao, W. Pan, C. Wan, Z. Qu, Z. Li, J. Yang, Defect engineering in development of low thermal conductivity materials: a review, *J. Eur. Ceram. Soc.* 37 (2017) 1–13.

[28] INVESTIGATION OF PHYSICAL PROPERTIES OF PYROCHLORE IRIDATES a thesis submitted by Kshiti Mishra.

[29] Telang, Prachi, Kshiti Mishra, Giacomo Prando, A. K. Sood, and Surjeet Singh. "Anomalous lattice contraction and emergent electronic phases in Bi-doped  $\text{Eu}_2\text{Ir}_2\text{O}_7$ ." *Physical Review B* 99, no. 20 (2019): 201112.

[30] Akhbarifar, Sepideh. "Quantum Physical Interpretation of Thermoelectric Properties of Ruthenate Pyrochlores." *Thermoelectricity: Recent Advances, New Perspectives and Applications* (2022): 115.

[31] Yasukawa, Masahiro, Sadayuki Kuniyoshi, and Toshio Kono. "Thermoelectric properties of the  $\text{Bi}_{2-x}\text{Y}_x\text{Ru}_2\text{O}_7$  ( $x=0-2$ ) pyrochlores." *Solid state communications* 126, no. 4 (2003): 213-216.

[32] Michitaka OHTAKI, Recent aspects of oxide thermoelectric materials for power generation from mid-to-high temperature heat source, *Journal of the Ceramic Society of Japan*, 2011, Volume 119, Issue 1395, Pages 770-775, Released on J-STAGE November 01, 2011, Online ISSN 1348-6535, Print ISSN 1882-0743, <https://doi.org/10.2109/jcersj2.119.770>,

[33] M. Ohtaki, D. Ogura, K. Eguchi and H. Arai, *J. Mater. Chem.*, 4, 653656 (1994).

[34] D. Berardan, E. Guilmeau, A. Maignan and B. Raveau, *Solid State Commun.*, 146, 97101 (2008).

[35] M. Ohtaki, K. Araki and K. Yamamoto, *J. Electron. Mater.*, 38, 12341238 (2009).

[36] H. Ohta, S. Kim, Y. Mune, T. Mizoguchi, K. Nomura, S. Ohta, T. Nomura, Y. Nakanishi, Y. Ikuhara, M. Hirano, H. Hosono and K. Koumoto, *Nat. Mater.*, 6, 129134 (2007).